

[Click here to view linked References](#)

1 **New shock microstructures in titanite (CaTiSiO₅) from the peak ring**
2 **of the Chicxulub impact structure, Mexico**

3 Nicholas E. Timms¹, Mark A. Pearce², Timmons M. Erickson^{1,3}, Aaron J. Cavosie¹,
4 Auriol S.P. Rae^{4,5}, John Wheeler⁶, Axel Wittmann⁷, Ludovic Ferrière⁸, Michael H.
5 Poelchau⁵, Naotaka Tomioka⁹, Gareth S. Collins⁴, Sean P. S. Gulick¹⁰, Cornelia
6 Rasmussen¹⁰, Joanna V. Morgan⁴ and the IODP-ICDP Expedition 364 Scientists*

7 ¹ *The Institute for Geoscience Research (TIGeR), Space Science and Technology*

8 *Centre, School of Earth and Planetary Sciences, Curtin University, Perth, GPO Box*
9 *U1987, WA 6845, Australia*

10 ² *CSIRO Mineral Resources, Australian Resources Research Centre, 26 Dick Perry*

11 *Avenue, Kensington, WA 6151, Australia*

12 ³ *Jacobs – JETS, NASA Johnson Space Center, Astromaterials Research and*

13 *Exploration Science Division, Mailcode XI3, 2101 NASA Parkway, Houston, TX, USA*

14 ⁴ *Department of Earth Science and Engineering, Imperial College London, London,*

15 *UK*

16 ⁵ *Institut für Geo- und Umweltwissenschaften, Albert-Ludwigs-Universität,*

17 *Freiburg, Albertstraße 23b, 79104 Freiburg, Germany*

18 ⁶ *Department of Earth and Ocean Sciences, University of Liverpool, Liverpool, L69*

19 *3GP, UK*

20 ⁷ *Eyring Materials Center, Arizona State University, Tempe, AZ, USA*

21 ⁸ *Natural History Museum, Vienna, Austria*

22 ⁹ *Kochi Institute for Core Sample Research, Japan Agency for Marine-Earth Science*
23 *and Technology, Kochi, Japan.*

24 ¹⁰ *Institute for Geophysics and Department of Geological Sciences, Jackson School of*
25 *Geosciences, University of Texas at Austin, Austin, TX, USA*

26 **See full list and affiliations at the end of the manuscript text file.*

27

28

29 **ABSTRACT**

30 Accessory mineral geochronometers such as apatite, baddeleyite, monazite, xenotime
31 and zircon are increasingly being recognized for their ability to preserve diagnostic
32 microstructural evidence of hypervelocity-impact processes. To date, little is known
33 about the response of titanite to shock metamorphism, even though it is a widespread
34 accessory phase and a U-Pb geochronometer. Here we report two new mechanical
35 twin modes in titanite within shocked granitoid from the Chicxulub impact structure,
36 Mexico. Titanite grains in the newly acquired core from the International Ocean
37 Discovery Program Hole M0077A preserve multiple sets of polysynthetic twins, most
38 commonly with composition planes $(K_1) = \sim\{\bar{1}11\}$, and shear direction $(\eta_1) = \langle 110 \rangle$,
39 and less commonly with the mode $K_1 = \{130\}$, $\eta_1 = \sim\langle 522 \rangle$. In some grains, $\{130\}$
40 deformation bands have formed concurrently with the deformation twins, indicating
41 dislocation slip with Burgers vector $\mathbf{b} = \langle 341 \rangle$ can be active during impact
42 metamorphism. Titanite twins in the modes described here have not been reported
43 from endogenically-deformed rocks; we therefore propose that these newly identified
44 twin form as a result of shock deformation. Formation conditions of the twins has not
45 been experimentally calibrated, and is here empirically constrained by the presence of
46 planar deformation features in quartz (12 ± 5 and $\sim 17 \pm 5$ GPa) and the absence of
47 shock twins in zircon (< 20 GPa). While the lower threshold of titanite twin formation
48 remains poorly-constrained, identification of these twins highlight the utility of
49 titanite as a shock indicator over the pressure range between 12-17 GPa. Given the
50 challenges to find diagnostic indicators of shock metamorphism to identify both

1
2
3
4
5
6
7
8
9
10
11
12
13
14
15
16
17
18
19
20
21
22
23
24
25
26
27
28
29
30
31
32
33
34
35
36
37
38
39
40
41
42
43
44
45
46
47
48
49
50
51
52
53
54
55
56
57
58
59
60
61
62
63
64
65
66
67
68
69
70
71
72
73
74
75
76

ancient and recent impact evidence on Earth, microstructural analysis of titanite is here demonstrated to provide a new tool for recognizing impact deformation in rocks where other impact evidence may be erased, altered, or did not manifest due to generally low (<20 GPa) shock pressure.

KEYWORDS: titanite, shock metamorphism, mechanical twinning, dislocation slip system, meteorite impact, EBSD

INTRODUCTION

Identifying and dating impacts is essential to understand their role in key processes in Earth history, such as mass extinctions (e.g. Hildebrand et al. 1991) and even the proposed relation to the onset of plate tectonics (O'Neill et al. 2017). Recent crystallographic and microstructural studies of datable accessory minerals like zircon (e.g. Moser et al. 2011; Timms et al. 2012; Erickson et al. 2013; Cavosie et al. 2016a; Cavosie et al. 2018a; Crow et al. 2018), monazite (e.g. Erickson et al. 2016; Erickson et al. 2017a), baddeleyite (e.g. Darling et al. 2016; Timms et al. 2017a; White et al. 2018), and xenotime (Cavosie et al. 2016b) have greatly expanded the potential to both recognize and date impact events (e.g. Erickson et al. 2017b). Titanite (CaTiSiO_5) is a widely-utilized U-Pb geo- and thermochronometer that occurs in a broad range of potential target rock compositions (Frost et al. 2001), including metamorphic, sedimentary, and felsic to mafic igneous rocks. We report a detailed electron backscatter diffraction (EBSD) microstructural study of impact deformation in titanite, focusing on samples of shocked granitoid from the 2016 International Ocean Discovery Program (IODP)-International Continental scientific Drilling Program (ICDP) Expedition 364, that drilled the peak ring of the 200 km wide Chicxulub impact structure off the coast of the Yucatán Peninsula (Morgan et al.

1
2
3
4
5
6
7
8
9
10
11
12
13
14
15
16
17
18
19
20
21
22
23
24
25
26
27
28
29
30
31
32
33
34
35
36
37
38
39
40
41
42
43
44
45
46
47
48
49
50
51
52
53
54
55
56
57
58
59
60
61
62
63
64
65

77 2017). We further demonstrate how these features can be distinguished from
78 deformation of titanite due to endogenic tectonic stresses.

80 **Titanite crystallography, microstructure, and deformation**

81 Titanite, formerly known as sphene until renamed by the International
82 Mineralogical Association (Hey 1982), has the nominal formula CaTiSiO_5 , with an
83 atomic structure comprising chains of octahedral 6-fold Ti and 4-fold Si, with Ca
84 occupying a seven-fold site (Higgins and Ribbe 1976; Speer and Gibbs 1976). At
85 ambient pressure and temperature, titanite is monoclinic, and belongs to the space
86 group family $P2_1/a$ (Speer and Gibbs 1976; Taylor and Brown 1976). Above 496 °K
87 (223 °C), displacements of adjacent octahedral Ti chains define a transition to an
88 intermediate structure (Kunz et al. 1996). Above 825 °K (552 °C), or above ~3.5 GPa
89 at room temperature, further modification of the structure results in an orthorhombic
90 $A2/a$ symmetry that accommodates a volume reduction of 5.1% (Salje et al. 1993;
91 Kunz et al. 1996; Angel et al. 1999). Titanite melts at >1380 °C (Hayward and
92 Cecchetto 1982).

93 Titanite has good cleavage along $\{110\}$, and can form simple growth twins
94 parallel to (100) (Deer et al. 1982). Two sets of symmetrically equivalent,
95 polysynthetic lamellar mechanical (deformation) twins in titanite were first reported
96 by Mügge (1889), and have since been documented in rocks affected by high-strain
97 rates. Deformation twins were reported in samples affected by 0.5-0.8 GPa pressure
98 during nuclear tests (Borg 1970), and were subsequently produced in laboratory
99 experiments at 0.8 GPa (Borg and Heard 1972). The twin mode for deformation twins
100 was defined as $K_1 = \sim\{221\}$, $\eta_1 = \langle 110 \rangle$, where K_1 = twinning (or composition) plane
101 and η_1 = shear direction (Borg 1970). With a critically resolved shear stress of ~0.13

102 GPa at 500 °C, $\sim\{221\}\langle 110\rangle$ twinning can occur in titanite at typical endogenic
103 tectono-metamorphic conditions (Borg and Heard 1972; Bonamici et al. 2015).
104 Titanite can also undergo dislocation creep (Müller and Franz 2004; Bonamici
105 et al. 2015) and dynamic recrystallization (Papapavlou et al. 2017) in tectono-
106 metamorphic settings. Crystal-plastic deformation of titanite is not well studied.
107 Dislocations with Burgers vectors (\mathbf{b}) = [100], [011] and [0 $\bar{1}$ 1] have been reported in
108 titanite at eclogite facies, and easy glide of dislocations with $\mathbf{b} = \frac{1}{2}\langle 011\rangle$ that is
109 predicted to occur in the A2/a phase (Müller and Franz 2004). Recrystallised
110 subgrains with low- and high-angle boundaries have also been reported in
111 tectonically-deformed titanite (Bonamici et al. 2015; Papapavlou et al. 2017; Kirkland
112 et al. 2018).

113 Titanite grains have been experimentally dynamically shocked to 59 GPa
114 (Deutsch and Schärer 1990). However, the resulting microstructures were not
115 characterised in detail. Previously reported titanite microstructures in naturally
116 shocked rocks that did not involve quantitative approaches have been described
117 simply as ‘subplanar fractures’ (e.g. Koeberl et al. 1996; Papapavlou et al. 2018),
118 ‘planar fractures’ and ‘mechanical twinning’ (Biren and Spray 2011). In breccia from
119 the Ries crater, Germany, Chao (1968) reported weakly-developed planar features and
120 misoriented mosaic textures. Whereas Abadian (1972) reported dominant cleavage
121 along (111) and (110), less common cleavage in an irrational plane $\parallel(552)$, and fine
122 (1-2 μm wide) planar elements parallel to the {010} zones. Electron backscatter
123 diffraction analysis of titanite in target rocks from the Sudbury impact structure,
124 Canada, and Vredefort impact structure, South Africa, have been shown to be crystal-
125 plastically deformed, and to contain lamellar twins with $\sim 74^\circ / \langle 102\rangle$ host-twin
126 disorientation axes, and neoblasts (Papapavlou et al. 2018). However, twins identified

127 in these studies have not been indexed. Until now, no studies have focused on
128 quantitatively distinguishing the style of deformation features that form in titanite in
129 tectonic stress regimes from those that form during impact events, which is the focus
130 of this study.

131

132 **Geological background and samples**

133 This study investigates titanite from the ~66 Ma, 200 km Chicxulub impact
134 structure in the Gulf of Mexico, which is widely reported to have caused the K-Pg
135 mass extinction (Hildebrand et al. 1991; Schulte et al. 2010; Renne et al. 2013). It is
136 one of the three largest known terrestrial impact structures (Grieve and Therriault
137 2000) and contains a well-preserved peak ring (Fig. 1) (Morgan et al. 1997; Gulick et
138 al. 2008; Gulick et al. 2013; Morgan et al. 2016; Riller et al. 2018). In 2016, IODP-
139 ICDP Expedition 364 drilled core from Hole M0077A (21° 27.009'N, 89° 56.962'W),
140 which penetrated the peak ring (Morgan et al. 2017) (Fig. 1). Recovered lithologies
141 include a section of shocked Paleozoic granitoid basement rocks from depths of 747-
142 1335 meters below sea floor (mbsf) that contain pre-impact mafic and felsic dike
143 lithologies as well as intercalations of impact breccia and impact melt rocks (Fig. 1)
144 (Morgan et al. 2017).

145 The granitic target rocks are coarse-grained and primarily composed of alkali
146 feldspar, quartz, plagioclase, minor biotite, and accessory muscovite, apatite, titanite,
147 epidote, magnetite, ilmenite, and zircon (Gulick et al. 2017; Morgan et al. 2017;
148 Schmieder et al. 2017). Most quartz grains contain multiple decorated planar
149 deformation features (PDFs), planar fractures (PFs), and feather features (FFs) (Fig.
150 2) (e.g. Ferrière et al. 2017; Gulick et al. 2017; Morgan et al. 2017; Rae et al. 2017;
151 Zhao et al. 2017; Rae 2018). Preliminary universal stage (U-stage) analysis of PDF

1
2
3
4
5
6
7
8
9
10
11
12
13
14
15
16
17
18
19
20
21
22
23
24
25
26
27
28
29
30
31
32
33
34
35
36
37
38
39
40
41
42
43
44
45
46
47
48
49
50
51
52
53
54
55
56
57
58
59
60
61
62
63
64
65

152 orientations in shocked quartz constrains the bulk shock pressure of rocks in the core
153 to $\sim 12 \pm 5$ to 17 ± 5 GPa (Rae et al. 2017; Feignon et al. 2018; Rae 2018). Titanite
154 grains up to 2 mm long occur as inclusions within all major phases of the granitic
155 rocks, including shocked quartz, and are often spatially associated with and/or include
156 other accessory phases, such as zircon and apatite (Figs. 2, 3).

157

158 **ANALYTICAL METHODS**

159 **Samples and approach used in this study**

160 Titanite grains and associated phases were characterised via optical
161 microscopy, backscattered electron (BSE) imaging, and EBSD mapping in thin
162 sections of three shocked granite core samples from Hole M0077A (364-77-A-121-R-
163 1-75-77, 364-77-A-204-R-1-7-9, and 364-77-A-219-R-1-22-24) from depths of
164 814.85, 1030.00, and 1076.16 metres below sea floor (mbsf), respectively (Figs. 2, 3,
165 and Table 1). The samples are referred to throughout this study by these depths with #
166 prefix (Table 1). Modes of twinning in titanite identified from EBSD data were
167 determined via analysis of the host-twin crystallographic orientation relationships. A
168 MATLAB script was used to determine the directions defining 180° misorientation
169 relationships, which correspond to either the twinning direction of shear (η_1) or the
170 pole to the compositional plane (twin plane, K_1) (Christian and Mahajan 1995;
171 Erickson et al. 2016). Finally, twins were indexed using geometric considerations
172 (Christian and Mahajan 1995) combined with the traces of twin lamellae on EBSD
173 maps. The geometry of low-angle lattice distortions associated with deformation
174 bands seen in EBSD data were analysed, including automated calculation of the
175 weighted Burgers vector (Wheeler et al. 2009).

176

177 **Scanning electron microscopy and electron backscatter diffraction mapping**
178 Prior to scanning electron microscopy, thin sections were polished progressively with
179 diamond paste to 0.5 μm , then given a final polish using 0.06 μm colloidal silica in
180 NaOH on a Buehler Vibromet II for four hours. A thin carbon coat was applied to
181 mitigate charging. Backscattered electron images were collected using a Tescan
182 MIRA3 field emission scanning electron microscope (FE-SEM) in the John de Laeter
183 Centre at Curtin University. Phases and their crystallographic microstructures were
184 quantified using combined energy dispersive X-ray (EDX) and electron backscatter
185 diffraction (EBSD) mapping using an Oxford Instruments AZtec system on the
186 Tescan MIRA3 FE-SEM at Curtin University. Data acquisition settings and
187 processing procedures followed those of Timms et al. (2017b) and are detailed in
188 Table 2. EBSD data were processed using the Tango and Mambo modules of Oxford
189 Instruments Channel 5.10 to produce thematic maps and pole figures, respectively.

191 **Determining twin modes from EBSD data**

192 EBSD mapping involves quantification of the crystallographic orientation of
193 phases relative to the sample surface. It is conventional to describe this absolute
194 crystallographic orientation in the x-y-z sample reference frame at a given x-y point
195 on the map as a sequence of three rotations from a reference orientation, known as
196 Euler angles ϕ_1 , Φ , and ϕ_3 (Bunge 1981; Prior et al. 1999). Twins are recognised in
197 EBSD maps as domains with a specific systematic misorientation relationship relative
198 to the host grain. Misorientation is defined as the rotation around an axis by some
199 angle that would bring any two differently orientated crystals into alignment (Wheeler
200 et al. 2001). Due to the symmetry of crystals, multiple misorientation axes are present.
201 Each axis corresponds to a different angular rotation, and all of these orientations

1
2
3
4
5
6
7
8
9
10
11
12
13
14
15
16
17
18
19
20
21
22
23
24
25
26
27
28
29
30
31
32
33
34
35
36
37
38
39
40
41
42
43
44
45
46
47
48
49
50
51
52
53
54
55
56
57
58
59
60
61
62
63
64
65

202 describe the relationship between the two domains. The most commonly reported type
203 of misorientation in EBSD data sets is the axis around which the minimum rotation is
204 required for realignment, which is specified as the disorientation (Wheeler et al.
205 2001). This distinction is important when considering mechanical twinning, where it
206 is conventional to classify twin modes based on rotations around axes where the
207 misorientation angle is 180° , and which may be different to the disorientation.

208 Deformation twins are characterized using one or both of the twinning /
209 composition plane, K_1 , and shear direction, η_1 , which results in 180° misorientation
210 relationships (Christian and Mahajan 1995). Deformation twins can be classified in
211 one of three ways. Type 1 twins have a rational K_1 , the pole to which is a
212 misorientation axis with rotation angle of 180° , and an irrational η_1 . Conversely, type
213 2 twins have rational η_1 , around which is a misorientation axis with the rotation angle
214 of 180° , and an irrational K_1 , and compound twins are defined by both rational K_1 and
215 η_1 , both of which are misorientation axes with rotations of 180° (Christian and
216 Mahajan 1995). In general, the relationship reported by EBSD software will not have
217 a rotation angle of 180° , as there will usually be a lower angle disorientation
218 relationship. The exceptions to this issue are in triclinic minerals (where there is only
219 one symmetric equivalent) and compound twins in monoclinic minerals (where there
220 are two symmetric equivalents and therefore they must both be components of the
221 twinning). This relationship means it is possible for the disorientation angle/axis to
222 bear no resemblance to K_1 and η_1 for various twin modes in most crystal systems.

223 A more sophisticated analysis of EBSD data that involved calculating 180°
224 misorientations is required to identify K_1 and η_1 for twinning in monoclinic phases
225 such as monazite (Erickson et al. 2016). A MATLAB script was developed that
226 utilizes Euler angle triplets for two representative data points from the host and

1
2
3
4
5
6
7
8
9
10
11
12
13
14
15
16
17
18
19
20
21
22
23
24
25
26
27
28
29
30
31
32
33
34
35
36
37
38
39
40
41
42
43
44
45
46
47
48
49
50
51
52
53
54
55
56
57
58
59
60
61
62
63
64
65

227 adjacent twin domain derived from the EBSD map, crystal unit cell parameters, and
228 Laue group symmetry operators as input parameters (Table 3).

229 First, the rotation matrix (\mathbf{R}), which describes the orientation relative to a
230 reference orientation, is calculated for each Euler triple (host \mathbf{R}_h , twin \mathbf{R}_t) using
231 equations B2 and B4 of Cho et al. (2005). These can be used to calculate the
232 directions in sample coordinates of particular crystal directions. For our purposes we
233 require a matrix which describes the rotation from host to twin *expressed in crystal*
234 *coordinates* ($\mathbf{R}_m = \mathbf{R}_h^{-1}\mathbf{R}_t$). Since this is in crystal coordinates, we derive rotation
235 matrices for each symmetric equivalent ($\mathbf{R}_m i = \mathbf{S}_i \mathbf{R}_m$) where \mathbf{S}_i is the i -th member of
236 the set of symmetry operators for the Laue class under consideration. The 180°
237 misorientation axes were calculated as angle/axis pairs in Cartesian x-y-z coordinates
238 (the sample reference frame). These were used to find best-fit crystallographic forms
239 using the dot product of unit vectors, as $\langle hkl \rangle$ or pole to $\{hkl\}$, implementing integer
240 search limits of $\bar{4}$ to 4 for h , k , and l to yield low-index (rational) best-fit forms.

241 Output data were compiled giving the crystallographic vector with the smallest value
242 normalised to 1 and their corresponding angular deviation from the calculated
243 misorientation axis. The orientation of K_1 , η_1 and S were reconstructed using a
244 stereographic projection, ensuring that the appropriate symmetric variants of K_1 and
245 η_1 were chosen such that its great circle contains the mapped x-y trace of the twins
246 and η_1 .

247 The K_1 and η_1 components of twin modes were deemed to be rational if
248 angular deviation between the calculated misorientation axis and the best-fit low
249 index crystallographic form were $<0.7^\circ$, which is a reasonable value given the mean
250 angular deviation associated with indexing EBSD data points is typically on the order
251 of 0.3 to 0.8° . Twin mode components were considered irrational where angular

1
2
3
4
5
6
7
8
9
10
11
12
13
14
15
16
17
18
19
20
21
22
23
24
25
26
27
28
29
30
31
32
33
34
35
36
37
38
39
40
41
42
43
44
45
46
47
48
49
50
51
52
53
54
55
56
57
58
59
60
61
62
63
64
65

252 deviation to the best-fit low-index form were $>0.7^\circ$ (typically $>1.5^\circ$). These results
253 were used to classify twin modes as types 1, 2, or compound twins, as described
254 above (Christian and Mahajan 1995). Results are summarized in Tables 4 and 5. For a
255 given twin mode, the disorientation axis is assumed to be defined by the intersection
256 of planes normal to η_1 for both symmetrically equivalent sets of twins. Therefore, the
257 disorientation axis associated with $\sim\{221\} \langle 110 \rangle$ twins (Borg 1970; Borg and Heard
258 1972) is parallel to $[102]$, which is coincident with the pole to (001) .

259

260 **Determination of slip systems**

261 Two approaches were used to determine dislocation slip systems active in
262 shocked titanite. The first approach involved a geometric analysis of crystal-plastic
263 deformation bands using EBSD data, assuming a simple tilt-boundary model, which
264 has been successfully applied to low-angle boundaries in other minerals (Boyle et al.
265 1998; Bestmann and Prior 2003; Reddy et al. 2007). This approach assumes that
266 disorientation axes associated with low-angle deformation bands are a consequence of
267 geometrically necessary dislocations, and that the disorientation axis, pole to the slip
268 plane, and Burgers vector (**b**) are orthonormal. Geometric reconstruction of low-angle
269 tilt boundary planes must contain their traces on EBSD maps and the disorientation
270 axis. The **b** is oriented normal to the tilt boundary, and the slip plane is assumed to
271 contain both **b** and the disorientation axis. The second approach involved automated
272 calculation of the weighted Burgers vector (WBV) of geometrically necessary
273 dislocations using orientation gradients in EBSD data (Wheeler et al. 2009). The
274 WBV is defined as the net Burgers vector of dislocations that intersect an area of the
275 EBSD map, and has been calculated by integration around the edge of a user-defined
276 area.

1
2
3
4
5
6
7
8
9
10
11
12
13
14
15
16
17
18
19
20
21
22
23
24
25
26
27
28
29
30
31
32
33
34
35
36
37
38
39
40
41
42
43
44
45
46
47
48
49
50
51
52
53
54
55
56
57
58
59
60
61
62
63
64
65

277 In this study, an automated version of the integral approach of Wheeler et al.
278 (2009) was implemented, whereby an EBSD map is automatically tiled into square,
279 20 x 20 pixel (6 x 6 μm) areas, and the WBV calculated for each tile. This method
280 reduces the errors on WBV in comparison to values calculated at every pixel. Results
281 from tiles were disregarded if the square overlapped a high-angle boundary (including
282 twin interfaces) or where the magnitude of the WBV length was below a threshold
283 value (i.e., a minimum dislocation density, $d_{\text{min}} = 0.001 (\mu\text{m})^{-1}$). The two
284 approaches to deducing dislocation slip systems described above are complementary:
285 the WBV approach is automated and does not involve assumptions about low-angle
286 boundary geometry, whereas the low-angle boundary model also allows indexing of
287 low-angle deformation bands.

288

289 **RESULTS**

290 **Microstructures in Chicxulub Titanite**

291 Four titanite grains were analysed, including a >1 mm long grain in #814.85; a
292 200 μm grain in #1030.00; and two grains from #1076.16 that are 300 μm and 500 μm
293 across, respectively (Figs. 2, 3). The titanite grains occur as inclusions within shocked
294 and fractured alkali feldspar and quartz, and are cut by brittle fractures (Figs. 2-7).
295 None of the studied grains occur in discrete breccia, melt, or cataclasite veins, and are
296 entirely enclosed within granitoid (Fig. 2). Surrounding quartz grains contain multiple
297 sets of PDFs, PFs, FFs (Fig. 2), and high densities of lobate/irregular Dauphiné twins
298 (Figs. 6, 7). Calcite and TiO_2 are commonly present along fractures in titanite and
299 along grain boundaries (Figs. 3-7).

300 All titanite grains were indexed as $\text{P}2_1/\text{a}$, with no evidence of the $\text{A}2/\text{a}$
301 structure. All four titanite grains contain two or more sets of polysynthetic twin

1
2
3
4
5
6
7
8
9
10
11
12
13
14
15
16
17
18
19
20
21
22
23
24
25
26
27
28
29
30
31
32
33
34
35
36
37
38
39
40
41
42
43
44
45
46
47
48
49
50
51
52
53
54
55
56
57
58
59
60
61
62
63
64
65

302 lamellae (Figs. 4-7). Twin lamellae are typically a few micrometres wide, straight to
303 slightly kinked, and tapered. Others terminate against grain boundaries, fractures, or
304 other twins, and are unevenly developed across the grains (Figs. 4-7). In some grains,
305 conspicuous sub-planar partings are present along twin interfaces (e.g., Figs. 4, 5).
306 Each titanite grain contains two sets of twins that are disorientated from the host grain
307 by $\sim 74^\circ$ / [102] (labelled T1 and T2 in Figs. 4-7). The grain from sample #1030.00
308 contains a third set of twins with a disorientation relative to the host of $\sim 51^\circ$ / [001]
309 (labelled T3 in Fig. 7A).

310 All host domains in the titanite grains record variable degrees of intragrain
311 misorientation, up to $\sim 30^\circ$, which manifests as dispersion in pole figures (Figs. 4-7).
312 While some dispersion is attributed to rigid rotation of fractured blocks, a component
313 is linked to progressive distortion and broad deformation bands with indistinct
314 boundaries, which are the result of crystal-plasticity (e.g., Fig. 5). Significant
315 thickening of twins along deformation bands in titanite grain 1 in #1076.16 indicates
316 that the formation of these microstructures was coeval (Fig. 8). The high angle of the
317 twin planes to the polished surface for this sample (Fig. 8B) means that the true
318 thickness is observed, and the twin thickness is not merely an apparent thickness, due
319 to the plane of observation. The best-developed (strongest and most planar)
320 deformation bands in the analysed titanite grains are defined by systematic
321 crystallographic disorientation about an axis sub-parallel with the pole to {111} (Fig.
322 8A-B). The map traces of the deformation bands are geometrically consistent with
323 low-angle tilt boundaries along {130} that contain the disorientation axis (Fig. 8B).
324 This geometric configuration can be explained by dislocation glide with Burgers
325 vector $\mathbf{b} = [341]$. This result is supported by weighted Burgers vector analysis, which

1
2
3
4
5
6
7
8
9
10
11
12
13
14
15
16
17
18
19
20
21
22
23
24
25
26
27
28
29
30
31
32
33
34
35
36
37
38
39
40
41
42
43
44
45
46
47
48
49
50
51
52
53
54
55
56
57
58
59
60
61
62
63
64
65

326 shows WBV forms dominant clusters around [341] (Fig. 8C-E), which has not
327 previously been described in titanite.

328

329 **Indexing of Twins in Titanite**

330 The most common twins encountered in the Chicxulub titanite grains have
331 disorientation relative to the host of $\sim 74^\circ$ / [102], and 180° misorientation axes that
332 align with $\langle 110 \rangle$ of the host grains, which is coincidental with η_1 of twins described
333 by Borg (1970) (Twins 1 and 2 in Figs. 4-7; Table 5). However, reconstruction of the
334 composition plane (K_1) using the map trace of these twins is consistent within a few
335 degrees of $\{\bar{1}11\}$, rather than $\{221\}$ expected for Borg (1970) twins. Therefore, they
336 define two symmetric equivalents of a previously undescribed type 2 twin mode with
337 $K_1 =$ irrational $\sim\{\bar{1}11\}$, $\eta_1 =$ rational $\langle 110 \rangle$, and shear plane (S) = $\{112\}$ (Fig. 10,
338 Table 5). A geometric consequence of this host-twin orientation relationship is that it
339 results in coincidence of many crystallographic planes between twin and host that lie
340 normal to $\eta_1 \langle 110 \rangle$, the 180° misorientation axis (Figs. 4-7, Table 5).

341 Twins with $\sim 51^\circ$ / [001] disorientation were found in one grain (labelled T3 in
342 Fig. 7A). The 180° misorientation axis for these twins aligns with the pole to $\{130\}$,
343 which defines a previously undescribed twin mode $K_1 = \{130\}$, $\eta_1 =$ irrational
344 $\sim\langle 522 \rangle$, and S = $(10\bar{3})$ (Table 5; Fig. 7B, 10). Two symmetrically equivalent variants
345 are possible for this twin mode, which are classified as type 1 twins because they have
346 a rational K_1 (Christian and Mahajan 1995) (Fig. 10).

347 Distinguishing between the newly described type 2 $\sim\{\bar{1}11\}$ twins and the
348 established $\sim\{221\}$ twins requires care, because they have identical η_1 (parallel to
349 $\langle 110 \rangle$) and thus produce identical disorientation axis/angle relationships using EBSD
350 data (Fig. 10, Table 5). Therefore, correct indexing requires consideration of the trace

1
2
3
4
5
6
7
8
9
10
11
12
13
14
15
16
17
18
19
20
21
22
23
24
25
26
27
28
29
30
31
32
33
34
35
36
37
38
39
40
41
42
43
44
45
46
47
48
49
50
51
52
53
54
55
56
57
58
59
60
61
62
63
64
65

351 of twin planes on the EBSD map and η_1 to reconstruct K_1 (e.g., Figs. 4-7). Indexing of
352 the newly described type 1 $\{130\} \sim \langle 522 \rangle$ twins is straightforward because it can be
353 inferred from the disorientation angle/axis alone, as no other twins are known to have
354 similar relationships.

355

356 **Microstructures in Co-existing Zircon**

357 A total of eight zircon grains were analysed in the same thin sections as the
358 titanite grains, including zircon grains that occur as inclusions within the larger
359 shocked titanite grains (Fig 3A). The zircon grains are typically $<60 \mu\text{m}$ across,
360 euhedral to anhedral in shape, with some grains preserving evidence of growth
361 zoning. All of the grains are fractured, and most of the observed variations in
362 crystallographic orientation, shown by variations in colour in EBSD orientation maps
363 and pole figures in Fig. 9, are related to rotation of rigid blocks separated by fractures
364 (Fig. 9A, B, D, F, and G). However, the zircon grains preserve minor evidence ($<5^\circ$)
365 of crystal-plastic strain, seen as smooth, systematic gradients in orientation that are
366 not related to fractures (Fig. 9A, E, and H). No microstructures diagnostic of shock
367 metamorphism, such as $\{112\}$ twins, the high-pressure polymorph reidite, granular
368 neoblasts, or dissociation textures (e.g. Timms et al. 2017b), were detected in the
369 zircon grains analysed. If present, these microstructures would have been readily
370 detected by the EBSD analysis utilized in this study.

371

372 **DISCUSSION**

373 **New titanite twins in Chicxulub shocked granite**

374 The two twin types found in Chicxulub titanite described here have not been
375 reported previously in tectonically-deformed titanite, and we propose that they are a

1
2
3
4
5
6
7
8
9
10
11
12
13
14
15
16
17
18
19
20
21
22
23
24
25
26
27
28
29
30
31
32
33
34
35
36
37
38
39
40
41
42
43
44
45
46
47
48
49
50
51
52
53
54
55
56
57
58
59
60
61
62
63
64
65

376 product of shock metamorphism during hypervelocity impact conditions given the
377 occurrence in granitoid with well-documented quartz microstructures indicative of
378 shock pressures of about 12 to 17 GPa. Thus, our results offer new insights into how
379 titanite deforms in impact environments. The new twin modes are geometrically
380 distinct from previously established mechanical and/or growth twins in titanite (e.g.
381 Borg 1970) (Fig. 10, Tables 4 and 5). The most common twins in Chicxulub titanite
382 grains have irrational composition planes (K_1) that are within a few degrees of $\{\bar{1}11\}$,
383 and a rational $\eta_1 = \langle 110 \rangle$, and $(S) = \{112\}$. Chicxulub titanite grains typically have
384 two sets of $\sim\{\bar{1}11\} \langle 110 \rangle$ twins, which is the maximum number possible given the
385 monoclinic symmetry. One unusual aspect of $\sim\{\bar{1}11\} \langle 110 \rangle$ twins is that they share
386 an identical twin-host minimum misorientation (disorientation) relationship with
387 previously established $\sim\{221\} \langle 110 \rangle$ twins (e.g., Borg, 1970), and thus the two twin
388 types cannot be distinguished solely based on disorientation angle/axis measurements
389 provided by EBSD analysis. Identification of each twin type thus requires indexing of
390 the composition planes (twin planes), which we calculated using a MATLAB script.

391 A set of lamellar twins with a different host-twin disorientation
392 crystallographic relationship of $\sim 51^\circ / [001]$ was found in one Chicxulub grain
393 (labelled T3 in Fig. 2A). These twins represent a second previously undescribed twin
394 mode in titanite, whereby $K_1 = \{130\}$, $\eta_1 =$ irrational $\sim\langle 522 \rangle$, and $S = (10\bar{3})$ (Table
395 4; Fig. 7B, 9C). Indexing of the newly described $\{130\} \sim\langle 522 \rangle$ twins is
396 straightforward because it can be inferred from the disorientation angle/axis relations
397 provided by EBSD data.

398

399 **Concurrent deformation processes in titanite during shock metamorphism**

1
2
3
4
5
6
7
8
9
10
11
12
13
14
15
16
17
18
19
20
21
22
23
24
25
26
27
28
29
30
31
32
33
34
35
36
37
38
39
40
41
42
43
44
45
46
47
48
49
50
51
52
53
54
55
56
57
58
59
60
61
62
63
64
65

400 The thickening of $\sim\{\bar{1}11\} \langle 110 \rangle$ mechanical twins along $\{130\}$ deformation
401 bands clearly indicates that dislocations with \mathbf{b} $[341]$ occurred concurrently with
402 twinning (Fig. 8). Concurrent crystal-plasticity could potentially have affected
403 twinning in two different ways: (1) the widening of twins was mechanically
404 facilitated by $\{\bar{1}12\} [341]$ dislocation activity, and/or (2) the formation of
405 deformation bands locally re-orientated titanite into a more favourable orientation for
406 twinning with respect to the stress field of the shock wave. Given that the slip vector
407 for twinning and Burgers vector for dislocation glide are similarly-oriented (i.e.,
408 twinning $\eta_1 = \langle 110 \rangle$ and dislocation $\mathbf{b} = \langle 341 \rangle$, respectively, are within $\sim 10^\circ$ of one
409 another), it is possible that these two types of microstructure have accommodated
410 shock deformation in a coherent and systematic way similar to cross slip. However,
411 the effects of localised re-orientation in deformation bands on the ease of twinning
412 cannot be resolved without additional information about the nature of the stress-strain
413 field associated with the passing shock wave relative to the orientation of the grains
414 and critically-resolved shear stress for twinning. Nevertheless, the absence of $\{130\}$
415 deformation bands in other shock-twinned grains in this study indicates that
416 concurrent $[341]$ dislocation slip is not a requirement for these twin modes in titanite.

417 418 **Petrological implications of the new twin modes in titanite**

419 Titanite in the target rocks that formed the peak ring at the Chicxulub crater
420 responded to the $\sim 12\text{--}17$ GPa bulk peak shock pressure principally by $\sim\{\bar{1}11\} \langle 110 \rangle$
421 twinning, with minor $\{130\} \sim\langle 522 \rangle$ twinning and coeval crystal-plasticity. Zircon, a
422 tetragonal accessory phase, is also known to form deformation twins and other
423 microstructures during shock deformation (Fig. 11). In contrast to titanite, zircon
424 grains in the same samples do not record diagnostic shock/impact-related

1
2
3
4
5
6
7
8
9
10
11
12
13
14
15
16
17
18
19
20
21
22
23
425 microstructures (Fig. 9), which is consistent with their having experienced shock
426 pressure <20 GPa (e.g. Timms et al. 2017b). In this respect, titanite appears similar to
427 xenotime, which has also been shown by empirical calibration with quartz and zircon
428 to form impact-related deformation twins and plastic deformation at shock pressures
429 <20 GPa (Cavosie et al. 2016b) (Fig. 11). Differences in the response of titanite and
430 other accessory minerals to shock deformation are shown in Fig. 11. The variable
431 microstructural responses are presumably related to the intrinsic material properties of
432 the different minerals, such as elasticity and yield strength for various failure modes,
433 which are largely controlled by crystal structure. Phase transformations and reactions
434 that determine phase stability through shock conditions are also important.

24
25
26
27
28
29
30
31
32
33
34
35
36
37
38
39
40
41
42
43
44
45
46
47
48
49
50
51
52
435 The precise details of the kinetics, nucleation stress, and critically resolved
436 shear stress for the newly described twin modes are yet to be determined by
437 theoretical or experimental means. However, unlike for shock twinning and
438 dislocations in zircon (Timms et al. 2018), theoretical calculations are inhibited by the
439 current lack of published elastic constants for P2₁/a titanite. More rigorous
440 investigations into the shock response of titanite via laboratory shock deformation
441 experiments remain an avenue for future research. Furthermore, very few quantitative
442 microstructural studies of naturally deformed titanite from tectonic and/or impact
443 environments are currently available (Papapavlou et al. 2017; Papapavlou et al. 2018).
444 Thus, further studies of naturally shocked and tectonically-deformed titanite are
445 required to provide better constraints on formation conditions for different twin
446 modes.

53
54
55
56
57
58
59
60
61
62
63
64
65
447 The discovery of new titanite twin modes in shocked target rocks at Chicxulub
448 represents the first steps toward developing a twin-based framework for using titanite
449 to distinguish tectonic versus impact-related deformation, similar to the approach

1
2
3
4
5
6
7
8
9
10
11
12
13
14
15
16
17
18
19
20
21
22
23
24
25
26
27
28
29
30
31
32
33
34
35
36
37
38
39
40
41
42
43
44
45
46
47
48
49
50
51
52
53
54
55
56
57
58
59
60
61
62
63
64
65

450 developed recently for monazite (Erickson et al. 2016). Titanite appears to behave
451 similarly to monazite in that a range of twin modes have been reported, with empirical
452 studies indicating that certain twin types uniquely form as a consequence of shock
453 deformation. Cleavage along $\sim\{\bar{1}11\}$ twin planes shown by several of the Chicxulub
454 grains is different to the dominant cleavage orientations reported for titanite from the
455 Ries crater (Abadian 1972). If titanite commonly cleaves along twin lamellae, then
456 observations of cleavage made by Abadian (1972) may be an indication that
457 additional shock twin modes could be revealed via detailed studies of shocked titanite
458 from other impact structures (Papapavlou et al. 2018). Our findings further indicate
459 that additional information is required to singular twin disorientation axes produced
460 from EBSD data in order to correctly index twins in titanite.

461

462 **Broader applications of deformation twin systematics**

463 In this study, we outline an approach for rigorous indexing and classification
464 of deformation twins from EBSD data based on geometric considerations of Christian
465 and Mahajan (1995). We demonstrate the importance of our approach for
466 distinguishing twin modes in titanite formed in tectonic versus shock settings. This
467 approach builds on the method outlined by Erickson et al. (2016) that led to the
468 discovery of new twin modes in monazite, and can be applied to other minerals that
469 form twins, such as ilmenite, rutile, and pyrrhotite, which could be useful for better
470 understanding deformation of rocks in both tectonic and impact settings.

471

472 **CONCLUSIONS**

473 In conclusion, titanite is a common accessory phase in a variety of rock types
474 (Frost et al. 2001), which has the propensity to record impact-related microstructures.

1
2
3
4
5
6
7
8
9
10
11
12
13
14
15
16
17
18
19
20
21
22
23
24
25
26
27
28
29
30
31
32
33
34
35
36
37
38
39
40
41
42
43
44
45
46
47
48
49
50
51
52
53
54
55
56
57
58
59
60
61
62
63
64
65

475 Specifically, we demonstrate titanite undergoes shock-related deformation twinning
476 along $\sim\{\bar{1}11\}$ and $\{130\}$, as recorded in the shocked target rocks of the Chicxulub
477 impact structure over the pressure range between 12 ± 5 and $\sim 17 \pm 5$ GPa. These twin
478 modes can form concurrently with deformation bands along $\{130\}$ resulting from
479 dislocation migration with a $\langle 341 \rangle$ Burgers vector. The newly-described twin modes
480 in $\sim\{\bar{1}11\}$ and $\{130\}$ are different from previously reported $\sim\{221\}$ twins from
481 tectonically-deformed titanite, and we therefore hypothesize that they are indicative of
482 shock conditions. We have defined geometric criteria for distinguishing these various
483 twins in titanite, which highlights the importance of utilizing a rigorous approach for
484 indexing twins. Furthermore, as this accessory mineral may be susceptible to age-
485 resetting during deformation (Papapavlou et al. 2017; Papapavlou et al. 2018), we
486 propose that our findings greatly increase the potential of titanite as a diagnostic
487 recorder of impact events in the geological record.

488

489 **ACKNOWLEDGEMENTS**

490 The Chicxulub drilling expedition was funded by the IODP as Expedition 364 with
491 co-funding from the ICDP, implementation by ECORD, and contributions and
492 logistical support from the Yucatán state government and UNAM. This research used
493 samples provided by the IODP, funding provided by a UK IODP NERC grant
494 (NE/P011195/1), and a Tescan Mira3 FE-SEM (ARC LE130100053) at the John de
495 Laeter Centre, Curtin University. ASPR received support from the Barringer Family
496 Fund for Meteorite Impact Research and STFC (ST/J001260/1), and thanks R.A.F.
497 Grieve and G.R. Osinski for their support. AJC acknowledges support from the
498 NASA Astrobiology program (grant #NNA13AA94A) and a Curtin Senior Research
499 Fellowship. TME acknowledges support from a Lunar and Planetary Institute

1
2
3
4
5
6
7
8
9
10
11
12
13
14
15
16
17
18
19
20
21
22
23
24
25
26
27
28
29
30
31
32
33
34
35
36
37
38
39
40
41
42
43
44
45
46
47
48
49
50
51
52
53
54
55
56
57
58
59
60
61
62
63
64
65

500 Postdoctoral Research Fellowship, the Center for Lunar Science and Exploration, and
501 D. Kring. AW, SG, and CR are supported by National Science Foundation (OCE-
502 1737087 and 1737351). This is UTIG Contribution #XXXX. J. Darling, W.U.
503 Reimold, and two anonymous reviewers are thanked for their comments on earlier
504 versions of the manuscript. We thank D. Rubatto for editorial handling.

505

506 **FIGURE CAPTIONS**

507 **Figure 1.** A. Gravity anomaly map of the Chicxulub impact structure showing traces
508 of various morphological features of the buried crater (dashed lines), location of Hole
509 M0077A, and sinkholes (cenotes) (white dots), and present-day coastline (solid white
510 line). B. Schematic core log of Hole M0077A showing the distribution of lithologies
511 and locations of samples used in this study. After Morgan et al. (2016) and Gulick et
512 al. (2013).

513

514 **Figure 2.** Optical photomicrographs of the samples used in this study. Mineral
515 abbreviations after Whitney and Evans (2009) include: Qz = quartz; Afs = alkali
516 feldspar; Pl = plagioclase; Ttn = titanite; Chl = chlorite; Bt = biotite. A. #814.85. B.
517 #1030.00. C. #1076.16. D. Region of interest in #1076.16 shown by white box in C.
518 White arrows annotate significant fracture orientations. Samples were impregnated
519 with blue epoxy prior to thin sectioning to enable the porosity to be visualized. Plane
520 polarized light images.

521

522 **Figure 3.** Backscattered electron images of titanite grains. Mineral abbreviations after
523 Whitney and Evans (2009) include: Qz = quartz; Afs = alkali feldspar; Pl =
524 plagioclase; Ttn = titanite; Zrn = zircon; Cal = calcite; Ap = apatite; Mag = magnetite;

1
2
3
4
5
6
7
8
9
10
11
12
13
14
15
16
17
18
19
20
21
22
23
24
25
26
27
28
29
30
31
32
33
34
35
36
37
38
39
40
41
42
43
44
45
46
47
48
49
50
51
52
53
54
55
56
57
58
59
60
61
62
63
64
65

525 Bt = biotite; Hc = hercynite. A. K-feldspar-hosted titanite in #814.85 shown in Fig.
526 2A. B. Detail of the margin of the titanite grain in A, showing a fractured zircon grain
527 and five sets of planar microstructures in alkali feldspar (black arrows). C. Primary
528 titanite, magnetite and apatite in a quartz domain in #1030.00 shown in Fig. 2B. D.
529 Apatite grains with planar fractures in an alkali feldspar domain in #1030.00. E.
530 Titanite in an alkali feldspar domain in #1076.16 shown in Fig. 2C. F. Titanite with
531 apatite, magnetite, zircon and hercynite in a quartz domain in #1076.16 shown in Fig.
532 2D. White arrows in A-F indicate the trace of transgranular fractures.

533

534 **Figure 4.** Microstructure of titanite grain from #814.85 (Fig. 3A). A. Cumulative
535 disorientation map showing 30° variation across the grain and two sets of twins
536 (labelled T1 and T2). An inclusion of a titanite grain with a different orientation is
537 shown by white outline labelled (i). B-C. Detailed maps of region shown in A. D.
538 Pole figures for (100), (010) and (001). Lower hemisphere, equal area projections in
539 the sample x-y-z reference frame. E. Crystallographic relationships between twin and
540 host for twins shown in A-C in the sample reference frame.

541

542 **Figure 5.** Microstructure of titanite grain 1 from #1076.16 (Fig. 3E). A. Cumulative
543 disorientation map showing 20° variation across the titanite grain and two sets of
544 twins (labelled T1 and T2). Fractures and perthitic lamellae are present in surrounding
545 K-feldspar grains. Inset (i) is a detailed map showing T2 twins. B. Pole figures for
546 (100), (010) and (001). Sparse systematically misindexed points at host-twin
547 interfaces (labelled as 's.m.') have disorientation relationships of $98^\circ / \langle \bar{2}\bar{1}2 \rangle$ and
548 $180^\circ / [003]$. Lower hemisphere, equal area projections in the sample x-y-z reference

1
2
3
4
5
6
7
8
9
10
11
12
13
14
15
16
17
18
19
20
21
22
23
24
25
26
27
28
29
30
31
32
33
34
35
36
37
38
39
40
41
42
43
44
45
46
47
48
49
50
51
52
53
54
55
56
57
58
59
60
61
62
63
64
65

549 frame. C. Crystallographic relationships between twin and host for twins shown in A
550 in the sample reference frame.

551
552 **Figure 6.** Microstructure of titanite grain 2 from #1076.16 (Fig. 3F). A. Cumulative
553 disorientation map showing 30° variation across the titanite grain and two sets of
554 twins (labelled T1 and T2). Dauphiné twins are present in surrounding quartz grains,
555 and magnetite contains thin lamellar twins. Inset (i) is a detailed map showing T2
556 twins. B. Pole figures for (100), (010) and (001). Lower hemisphere, equal area
557 projections in the sample x-y-z reference frame. C. Crystallographic relationships
558 between twin and host for twins shown in A in the sample reference frame.

559
560 **Figure 7.** A. EBSD map of titanite in sample #1030.00 from the Chicxulub crater
561 peak ring (Fig. 3C). Titanite is coloured for cumulative disorientation relative to
562 reference orientation (red cross) and has three sets of twins (T1, T2, and T3). It is
563 surrounded by quartz with Dauphiné twins (Qz, orange/red), calcite (Cal, yellow) and
564 TiO₂. Inset (i) shows pole figure for (100) in sample reference frame. B.
565 Crystallographic relationships between twins T1, T2, and T3 and host grain. Several
566 low-index poles to coincident planes (grey circles) align along the plane normal to η_1
567 for Twins 1 and 2. Lower hemisphere, equal area projections in the sample x-y-z
568 reference frame.

569
570 **Figure 8.** A. Detailed EBSD map of grain 1 from #1076.16 shown in Fig. 5. Titanite
571 is coloured for cumulative disorientation relative to reference orientation (red cross)
572 and twins (purple, labelled T1). Crystal-plastic deformation band (green-orange
573 domain) has a well-defined lower boundary trace (white dashed line), and is displaced

1
2
3
4
5
6
7
8
9
10
11
12
13
14
15
16
17
18
19
20
21
22
23
24
25
26
27
28
29
30
31
32
33
34
35
36
37
38
39
40
41
42
43
44
45
46
47
48
49
50
51
52
53
54
55
56
57
58
59
60
61
62
63
64
65

574 by brittle fractures. Twin lamellae are thicker within the deformation band. B.
575 Composite pole figure of data shown by the white box in A, plotted in the sample x-y-
576 z reference frame. Crystallographic data show a systematic dispersion about a
577 disorientation axis approximately parallel to the pole to (111). The deformation band
578 is consistent with a {130} tilt boundary geometry that contains the disorientation axis
579 and the trend of the deformation band on the polished surface. The dominant
580 dislocation slip system that contributed to the deformation bands involved glide with
581 a [341] Burgers vector. C EBSD map of the entire grain showing results of automated
582 weighted Burgers vector (WBV) analysis. Superimposed squares indicate 6 x 6 μm
583 tiles from which the integral WBV was calculated. Tiles that overlap with twin
584 domains have been disregarded. Tiles are coloured for WBV orientation using an
585 inverted pole figure (IPF) colour scheme. D Pole figure of WBV data shown in C,
586 plotted in crystallographic reference frame. E Contoured pole figure of data shown in
587 D, indicating dominance of WBV parallel to [341].

588
589 **Figure 9.** Microstructure of zircon grains associated with titanite from samples
590 #814.85 and #1030.00 of this study.

591
592 **Figure 10.** Summary of the geometric elements of deformation microstructures in
593 titanite. Pole Figures A. $\sim\{221\} \langle 110 \rangle$ twins after Borg (1970). B. $\sim\{\bar{1}11\} \langle 110 \rangle$
594 twins, this study. C. $\{130\} \sim\langle 522 \rangle$ twins, this study. D. $\{130\}$ deformation bands,
595 this study. The two possible symmetric equivalent variants are shown for each type of
596 microstructure. Microstructures shown in B, C, and D have not been described from
597 tectonically-deformed titanite.

1
2
3
4
5
6
7
8
9
10
11
12
13
14
15
16
17
18
19
20
21
22
23
24
25
26
27
28
29
30
31
32
33
34
35
36
37
38
39
40
41
42
43
44
45
46
47
48
49
50
51
52
53
54
55
56
57
58
59
60
61
62
63
64
65

599 **Figure 11.** Accessory phases as indicators of shock metamorphism. [1]: Leroux et al.
600 (1999), [2]: Timms et al. (2012), [3]: Moser et al. (2009), [4]: Timms et al. (2017a),
601 [5]: Erickson et al. (2013), [6]: Nemchin et al. (2009), [7]: Timms et al. (2018), [8]:
602 Moser et al. (2011), [9]: Thomson et al. (2014), [10]: Cox et al. (2018), [11]:
603 Wittmann et al. (2006), [12]: Cavosie et al. (2015b), [13]: Reddy et al. (2015), [14]:
604 Erickson et al. (2017a), [15]: Cavosie et al. (2015a), [16]: Cavosie et al. (2016a), [17]:
605 Cavosie et al. (2018b), [18]: Timms et al. (2017b), [19]: Erickson et al. (2015), [20]:
606 Erickson et al. (2016), [21]: Erickson et al. (2017b), [22]: Cavosie et al. (2016b), [23]:
607 Darling et al. (2016), [24]: White et al. (2018), [25]: Müller and Franz (2004), [26]:
608 Borg (1970), [27]: Papapavlou et al. (2018), [28]: Papapavlou et al. (2017). Note that
609 the pressures indicated are specifically mean (bulk) pressures for rocks with
610 negligible initial porosity, such as the granitoids in this study. The effects of porosity
611 on bulk shock pressure have been treated elsewhere (e.g., Güldemeister et al. 2013).

612

613

614

615 *** IODP-ICDP Expedition 364 Scientists**

616 S. P. S. Gulick¹, J. V. Morgan², E. Chenot³, G. L. Christeson⁴, P. Claeys⁵, C. S.
617 Cockell⁶, M. J. L. Coolen⁷, L. Ferrière⁸, C. Gebhardt⁹, K. Goto¹⁰, S. Green¹¹, H.
618 Jones¹², D. A. Kring¹³, J. Lofi³, C. M. Lowery⁴, R. Ocampo-Torres¹⁴, L. Perez-Cruz¹⁵,
619 A. E. Pickersgill^{16, 17}, M. H. Poelchau¹⁸, A. S. P. Rae^{2, 18}, C. Rasmussen^{4, 19}, M.
620 Rebolledo-Vieyra²⁰, U. Riller²¹, H. Sato²², J. Smit²³, S. M. Tikoo²⁴, N. Tomioka²⁵, J.
621 Urrutia-Fucugauchi¹⁵, M. T. Whalen²⁶, A. Wittmann²⁷, L. Xiao²⁸, K. E. Yamaguchi²⁹,
622 ³⁰.

1
2
3
4
5
6
7
8
9
10
11
12
13
14
15
16
17
18
19
20
21
22
23
24
25
26
27
28
29
30
31
32
33
34
35
36
37
38
39
40
41
42
43
44
45
46
47
48
49
50
51
52
53
54
55
56
57
58
59
60
61
62
63
64
65

623 ¹*Institute for Geophysics and Department of Geological Sciences, Jackson School of*
624 *Geosciences, University of Texas at Austin, Austin, TX, USA.* ²*Department of Earth*
625 *Science and Engineering, Imperial College London, London, UK.* ³ *Géosciences*
626 *Montpellier, Université de Montpellier, Montpellier, France.* ⁴*Institute for*
627 *Geophysics, Jackson School of Geosciences, University of Texas at Austin, Austin,*
628 *TX, USA.* ⁵*Analytical, Environmental and Geo-Chemistry, Vrije Universiteit Brussel,*
629 *Brussels, Belgium.* ⁶*Centre for Astrobiology, School of Physics and Astronomy,*
630 *University of Edinburgh, Edinburgh, UK.* ⁷*Department of Chemistry, WA-Organic*
631 *and Isotope Geochemistry Centre, Curtin University, Perth, Western Australia,*
632 *Australia.* ⁸*Natural History Museum, Vienna, Austria.* ⁹*Alfred Wegener Institute*
633 *Helmholtz Centre of Polar and Marine Research, Bremerhaven, Germany.*
634 ¹⁰*International Research Institute of Disaster Science, Tohoku University, Sendai,*
635 *Japan.* ¹¹*British Geological Survey, Edinburgh, UK.* ¹²*Department of Geo sciences,*
636 *Pennsylvania State University, University Park, PA, USA.* ¹³*Lunar and Planetary*
637 *Institute, Houston, TX, USA.* ¹⁴*Groupe de Physico-Chimie de l'Atmosphère, L'Institut*
638 *de Chimie et Procédés pour l'Énergie, l'Environnement et la Santé (ICPEES),*
639 *Université de Strasbourg, Strasbourg, France.* ¹⁵*Instituto de Geofísica, Universidad*
640 *Nacional Autónoma De México, Mexico, Mexico.* ¹⁶*School of Geographical and Earth*
641 *Sciences, University of Glasgow, Glasgow, UK.* ¹⁷*Argon Isotope Facility, Scottish*
642 *Universities Environmental Research Centre, East Kilbride, UK.* ¹⁸*Institut für Geo-*
643 *und Umweltnaturwissenschaften, Albert-Ludwigs-Universität, Freiburg, Germany.*
644 ¹⁹*Department of Geology and Geophysics, University of Utah, Salt Lake City, UT,*
645 *USA.* ²⁰*Independent consultant, Cancun, Mexico.* ²¹*Institut für Geologie, Universität*
646 *Hamburg, Hamburg, Germany.* ²²*Japan Agency for Marine-Earth Science and*
647 *Technology, Kanagawa, Japan.* ²³*Faculty of Earth and Life Sciences (FALW), Vrije*

1
2
3
4
5
6
7
8
9
10
11
12
13
14
15
16
17
18
19
20
21
22
23
24
25
26
27
28
29
30
31
32
33
34
35
36
37
38
39
40
41
42
43
44
45
46
47
48
49
50
51
52
53
54
55
56
57
58
59
60
61
62
63
64
65

648 *Universiteit Amsterdam, Amsterdam, Netherlands.* ²⁴*Earth and Planetary Sciences,*
649 *Rutgers University, New Brunswick, NJ, USA.* ²⁵*Kochi Institute for Core Sample*
650 *Research, Japan Agency for Marine-Earth Science and Technology, Kochi, Japan.*
651 ²⁶*Department of Geosciences, University of Alaska Fairbanks, Fairbanks, AK, USA.*
652 ²⁷*Eyring Materials Center, Arizona State University, Tempe, AZ, USA.* ²⁸*School of*
653 *Earth Sciences, Planetary Science Institute, China University of Geosciences, Wuhan,*
654 *China.* ²⁹*Department of Chemistry, Toho University, Chiba, Japan.* ³⁰*NASA*
655 *Astrobiology Institute.*

656

657 **REFERENCES CITED**

658

659

660 Abadian M (1972) Petrography, shock metamorphism and genesis of polymict
661 cristalline breccias in the Nordlinger Ries. Contributions to Mineralogy and Petrology
662 35(3):245

663 Angel RJ, Kunz M, Miletich R, Woodland AB, Koch M, Xirouchakis D (1999) High-
664 pressure phase transition in CaTiOSiO₄ titanite. Phase Transitions 68(3):533-543
665 doi:10.1080/01411599908224532

666 Bestmann M, Prior DJ (2003) Intragranular dynamic recrystallization in naturally
667 deformed calcite marble: diffusion accommodated grain boundary sliding as a result
668 of subgrain rotation recrystallization. Journal of Structural Geology 25(10):1597-1613
669 doi:10.1016/s0191-8141(03)00006-3

670 Biren MB, Spray JG (2011) Shock veins in the central uplift of the Manicouagan
671 impact structure: Context and genesis. Earth and Planetary Science Letters 303(3-
672 4):310-322 doi:10.1016/j.epsl.2011.01.003

1
2
3
4
5
6
7
8
9
10
11
12
13
14
15
16
17
18
19
20
21
22
23
24
25
26
27
28
29
30
31
32
33
34
35
36
37
38
39
40
41
42
43
44
45
46
47
48
49
50
51
52
53
54
55
56
57
58
59
60
61
62
63
64
65

673 Bonamici CE, Fanning CM, Kozdon R, Fournelle JH, Valley JW (2015) Combined
674 oxygen-isotope and U-Pb zoning studies of titanite: New criteria for age preservation.
675 *Chemical Geology* 398:70-84 doi:10.1016/j.chemgeo.2015.02.002
676 Borg IY (1970) Mechanical <110> twinning in shocked sphene. *American*
677 *Mineralogist* 55:1876-1888
678 Borg IY, Heard HC (1972) Mechanical twinning in sphene at 8 Kbar, 25° to 500° C.
679 *Geological Society of America Memoirs* 132:585-592
680 Boyle AP, Prior DJ, Banham MH, Timms NE (1998) Plastic deformation of
681 metamorphic pyrite: new evidence from electron-backscatter diffraction and
682 foreshatter orientation-contrast imaging. *Mineralium Deposita* 34(1):71-81
683 doi:10.1007/s001260050186
684 Bunge HJ (1981) Fabric analysis by orientation distribution functions.
685 *Tectonophysics* 78(1-4):1-21
686 Cavosie AJ, Erickson TM, Timms NE, Reddy SM, Talavera C, Montalvo SD, Pincus
687 MR, Gibbon RJ, Moser D (2015a) A terrestrial perspective on using ex situ shocked
688 zircons to date lunar impacts. *Geology* 43(11):999-1002 doi:10.1130/g37059.1
689 Cavosie AJ, Erickson TM, Timms NE (2015b) Nanoscale records of ancient shock
690 deformation: Reidite (ZrSiO₄) in sandstone at the Ordovician Rock Elm impact crater.
691 *Geology* 43(4):315-318 doi:10.1130/g36489.1
692 Cavosie AJ, Timms NE, Erickson TM, Hagerty JJ, Hörz F (2016a) Transformations
693 to granular zircon revealed: Twinning, reidite, and ZrO₂ in shocked zircon from
694 Meteor Crater. *Geology* 44(9):703-706
695 Cavosie AJ, Montalvo PE, Timms NE, Reddy SM (2016b) Nanoscale deformation
696 twinning in xenotime, a new shocked mineral, from the Santa Fe impact structure
697 (New Mexico, USA). *Geology* 44(10):803-806

1
2
3
4
5
6
7
8
9
10
11
12
13
14
15
16
17
18
19
20
21
22
23
24
25
26
27
28
29
30
31
32
33
34
35
36
37
38
39
40
41
42
43
44
45
46
47
48
49
50
51
52
53
54
55
56
57
58
59
60
61
62
63
64
65

698 Cavosie AJ, Timms NE, Erickson TM, Koeberl C (2018a) New clues from Earth's
699 most elusive impact crater: Evidence of reidite in Australasian tektites from Thailand.
700 *Geology* doi:10.1130/g39711.1

701 Cavosie AJ, Timms NE, Ferrière L, Rochette P (2018b) FRIGN zircon—The only
702 terrestrial mineral diagnostic of high - pressure and high - temperature shock
703 deformation. *Geology* 46(10):891-894 doi:10.1130/G45079.1

704 Chao ECT (1968) Pressure and temperature histories of impact metamorphosed
705 rocks—based on petrographic observations. In: French BM, Short NM (eds) *Shock
706 metamorphism of natural materials*, vol. Mono Press, Baltimore, Md, pp 135-158

707 Cho JH, Rollett AD, Oh KH (2005) Determination of a mean orientation in electron
708 backscatter diffraction measurements. *Metallurgical and Materials Transactions A*
709 36(12):3427-3438

710 Christian JW, Mahajan S (1995) Deformation twinning. *Progress in Materials Science*
711 39:1-57

712 Cox MA, Cavosie AJ, Bland PA, Miljković K, Wingate MTD (2018) Microstructural
713 dynamics of central uplifts: Reidite offset by zircon twins at the Woodleigh impact
714 structure, Australia. *Geology* doi:10.1130/g45127.1

715 Crow CA, Moser DE, McKeegan KD (2018) Shock metamorphic history of >4 Ga
716 Apollo 14 and 15 zircons. *Meteoritics & Planetary Science* doi:10.1111/maps.13184

717 Darling JR, Moser DE, Barker IR, Tait KT, Chamberlain KR, Schmitt AK, Hyde BC
718 (2016) Variable microstructural response of baddeleyite to shock metamorphism in
719 young basaltic shergottite NWA 5298 and improved U–Pb dating of Solar System
720 events. *Earth and Planetary Science Letters* 444:1-12 doi:10.1016/j.epsl.2016.03.032

721 Deer WA, Howie RA, Zussman J (1982) *Rock-Forming Minerals: Orthosilicates*,
722 Volume 1A (2nd Edition). Geological Society of London,

1 723 Deutsch A, Schärer U (1990) Isotope systematics and shock-wave metamorphism: I.
2 724 U-Pb in zircon, titanite and monazite, shocked experimentally up to 59 GPa.
3
4 725 *Geochimica et Cosmochimica Acta* 54(12):3427-3434
5
6 726 Erickson TM, Cavosie AJ, Moser DE, Barker IR, Radovan HA (2013) Correlating
7
8 727 planar microstructures in shocked zircon from the Vredefort Dome at multiple scales:
9
10 728 Crystallographic modeling, external and internal imaging, and EBSD structural
11
12 729 analysis. *American Mineralogist* 98(1):53-65 doi:10.2138/am.2013.4165
13
14 730 Erickson TM, Pearce MA, Taylor RJM, Timms NE, Clark C, Reddy SM, Buick IS
15
16 731 (2015) Deformed monazite yields high-temperature tectonic ages. *Geology* 43(5):383-
17
18 732 386 doi:10.1130/g36533.1
19
20 733 Erickson TM, Cavosie AJ, Pearce MA, Timms NE, Reddy SM (2016) Empirical
21
22 734 constraints on shock features in monazite using shocked zircon inclusions. *Geology*
23
24 735 44(8):635-638
25
26 736 Erickson TM, Pearce MA, Reddy SM, Timms NE, Cavosie AJ, Bourdet J, Rickard
27
28 737 WDA, Nemchin AA (2017a) Microstructural constraints on the mechanisms of the
29
30 738 transformation to reidite in naturally shocked zircon. *Contributions to Mineralogy and*
31
32 739 *Petrology* 172(1):6
33
34 740 Erickson TM, Timms NE, Kirkland CL, Tohver E, Cavosie AJ, Pearce MA, Reddy
35
36 741 SM (2017b) Shocked monazite chronometry: integrating microstructural and *in situ*
37
38 742 isotopic age data for determining precise impact ages. *Contributions to Mineralogy*
39
40 743 and *Petrology* 172(2-3):11 doi:10.1007/s00410-017-1328-2
41
42 744 Feignon J-G, Ferrière L, Koeberl C (2018) Petrography and shock metamorphism of
43
44 745 granitoid samples from the Chicxulub peak-ring IODP-ICDP expedition 364 drill
45
46 746 core. EGU General Assembly Conference Abstracts 20
47
48
49
50
51
52
53
54
55
56
57
58
59
60
61
62
63
64
65

1
2
3
4
5
6
7
8
9
10
11
12
13
14
15
16
17
18
19
20
21
22
23
24
25
26
27
28
29
30
31
32
33
34
35
36
37
38
39
40
41
42
43
44
45
46
47
48
49
50
51
52
53
54
55
56
57
58
59
60
61
62
63
64
65

747 Ferrière L, Rae ASP, Poelchau M, Koeberl C, Party at I-IES (2017) Macro- and
748 microscopic evidence of impact metamorphism in rocks from the Chicxulub peak ring
749 IODP-ICDP Expedition 364 drill core. In: 48th Lunar and Planetary Science
750 Conference, vol., The Woodlands, Texas, p 1600
751 Frost BR, Chamberlain KR, Schumacher JC (2001) Spinel (titanite): phase relations
752 and role as a geochronometer. *Chemical Geology* 172(1-2):131-148
753 Grieve R, Theriault A (2000) Vredefort, Sudbury, Chicxulub: three of a kind?
754 *Annual Review of Earth and Planetary Sciences* 28(1):305-338
755 Guldemeister N, Wünnemann K, Durr N, Hiermaier S (2013) Propagation of impact-
756 induced shock waves in porous sandstone using mesoscale modeling. *Meteoritics &*
757 *Planetary Science* 48(1):115-133 doi:10.1111/j.1945-5100.2012.01430.x
758 Gulick S, Morgan J, Mellett CL, Green SL, Bralower T, Chenot E, Christeson G,
759 Claeys P, Cockell C, Coolen MJL, Ferrière L, Gebhardt C, Goto K, Jones H, Kring D,
760 Lofi J, Lowery C, Ocampo-Torres R, Perez-Cruz L, Pickersgill AE, Poelchau M, Rae
761 A, Rasmussen C, Rebolledo-Vieyra M, Riller U, Sato H, Smit J, Tikoo S, Tomioka N,
762 Urrutia-Fucugauchi J, Whalen M, Wittmann A, Yamaguchi K, Xiao L, Zylberman W
763 (2017) Expedition 364 summary. In: Morgan J, Gulick S, Mellett CL, Green SL,
764 Scientists at E eds) *Proceedings of the International Ocean Discovery Program*, vol
765 364. College Station, TX (International Ocean Discovery Program), Texas, pp 1-23
766 Gulick SP, Barton PJ, Christeson GL, Morgan JV, McDonald M, Mendoza-Cervantes
767 K, Pearson ZF, Surendra A, Urrutia-Fucugauchi J, Vermeesch PM, Warner MR
768 (2008) Importance of pre-impact crustal structure for the asymmetry of the Chicxulub
769 impact crater. *Nature Geoscience* 1(2):131

1
2
3
4
5
6
7
8
9
10
11
12
13
14
15
16
17
18
19
20
21
22
23
24
25
26
27
28
29
30
31
32
33
34
35
36
37
38
39
40
41
42
43
44
45
46
47
48
49
50
51
52
53
54
55
56
57
58
59
60
61
62
63
64
65

770 Gulick SPS, Christeson GL, Barton PJ, Grieve RAF, Morgan JV, Urrutia-Fucugauchi
771 J (2013) Geophysical characterization of the Chicxulub impact crater. *Reviews of*
772 *Geophysics* 51(1):31-52 doi:10.1002/rog.20007
773 Hayward PJ, Cecchetto EV (1982) *Scientific Basis for Nuclear Waste Management.*
774 North Holland, Amsterdam
775 Hey MH (1982) International Mineralogical Association: commission on new
776 minerals and mineral names. *Mineralogical Magazine* 46(341):513-514
777 Higgins JB, Ribbe PH (1976) The crystal chemistry and space groups of natural and
778 synthetic titanites. *American Mineralogist* 61(9-10):878-888
779 Hildebrand AR, Penfield GT, Kring DA, Pilkington M, Camargo Z A, Jacobsen SB,
780 Boynton WV (1991) Chicxulub crater: a possible Cretaceous/Tertiary boundary
781 impact crater on the Yucatan Peninsula, Mexico. *Geology* 19(9):867-871
782 Kirkland CL, Fougereuse D, Reddy SM, Hollis J, Saxey DW (2018) Assessing the
783 mechanisms of common Pb incorporation into titanite. *Chemical Geology* 483:558-
784 566 doi:10.1016/j.chemgeo.2018.03.026
785 Koeberl C, Reimold WU, Kracher A, Träxler B, Vormaiier A, Körner W (1996)
786 Mineralogical, petrological, and geochemical studies of drill core samples from the
787 Manson impact structure, Iowa. *Geological Society of America Special Papers*
788 302(166)
789 Kunz M, Xirouchakis D, Lindsley DH, Hausermann D (1996) High-pressure phase
790 transition in titanite (CaTiOSiO₄). *American Mineralogist* 81(11-12):1527-1530
791 Leroux H, Reimold WU, Koerberl C, Hornemann U, Doukan J-C (1999)
792 Experimental shock deformation in zircon: a transmission electron microscopy study.
793 *Earth and Planetary Science Letters* 169:291-301

1
2
3
4
5
6
7
8
9
10
11
12
13
14
15
16
17
18
19
20
21
22
23
24
25
26
27
28
29
30
31
32
33
34
35
36
37
38
39
40
41
42
43
44
45
46
47
48
49
50
51
52
53
54
55
56
57
58
59
60
61
62
63
64
65

794 Morgan J, Warner M, Brittan J, Buffler R, Camargo A, Christeson G, Denton P,
795 Hildebrand A, Hobbs R, Macintyre H, Mackenzie G (1997) Size and morphology of
796 the Chicxulub impact crater. *Nature* 390(6659):472
797 Morgan J, Gulick S, Mellett CL, Green SL, Expedition364Scientists (2017)
798 Chicxulub: Drilling the K-Pg Impact Crater. Expedition 364 of the mission-specific
799 drilling platform from and to Progresso, Mexico. Site M0077. Proceedings of the
800 International Ocean Discovery Program 364
801 Morgan JV, Gulick SP, Bralower T, Chenot E, Christeson G, Claeys P, Cockell C,
802 Collins GS, Coolen MJ, Ferrière L, Gebhardt C (2016) The formation of peak rings in
803 large impact craters. *Science* 354(6314):878-882
804 Moser DE, Davis WJ, Reddy SM, Flemming RL, Hart RJ (2009) Zircon U–Pb strain
805 chronometry reveals deep impact-triggered flow. *Earth and Planetary Science Letters*
806 277(1-2):73-79 doi:10.1016/j.epsl.2008.09.036
807 Moser DE, Cupelli CL, Barker IR, Flowers RM, Bowman JR, Wooden J, Hart JR
808 (2011) New zircon shock phenomena and their use for dating and reconstruction of
809 large impact structures revealed by electron nanobeam (EBSD, CL, EDS) and isotopic
810 U–Pb and (U–Th)/He analysis of the Vredefort dome. *Canadian Journal of Earth*
811 *Sciences* 48(2):117-139 doi:10.1139/e11-011
812 Mügge O (1889) Über durch Druck entstandene Zwillinge von Titanit nach den
813 Kanten [110] und [HO]. , 11, 98. *Neues Jahrb Mineral, Geologie u Paläontologie*
814 11:98-115
815 Müller WF, Franz G (2004) Unusual deformation microstructures in garnet, titanite
816 and clinozoisite from an eclogite of the Lower Schist Cover, Tauern Window,
817 Austria. *European Journal of Mineralogy* 16(6):939-944 doi:10.1127/0935-
818 1221/2004/0016-0939

1
2
3
4
5
6
7
8
9
10
11
12
13
14
15
16
17
18
19
20
21
22
23
24
25
26
27
28
29
30
31
32
33
34
35
36
37
38
39
40
41
42
43
44
45
46
47
48
49
50
51
52
53
54
55
56
57
58
59
60
61
62
63
64
65

819 Nemchin A, Timms N, Pidgeon R, Geisler T, Reddy S, Meyer C (2009) Timing of
820 crystallization of the lunar magma ocean constrained by the oldest zircon. *Nature*
821 *Geoscience* 2(2):133-136 doi:10.1038/NGEO417
822 O'Neill C, Marchi S, Zhang S, Bottke W (2017) Impact-driven subduction on the
823 Hadean Earth. *Nature Geoscience* 10(10):793-797 doi:10.1038/ngeo3029
824 Papapavlou K, Darling JR, Storey CD, Lightfoot PC, Moser DE, Lasalle S (2017)
825 Dating shear zones with plastically deformed titanite: New insights into the orogenic
826 evolution of the Sudbury impact structure (Ontario, Canada). *Precambrian Research*
827 291:220-235 doi:10.1016/j.precamres.2017.01.007
828 Papapavlou K, Darling JR, Moser DE, Barker IR, White LF, Lightfoot PC, Storey
829 CD, Dunlop J (2018) U–Pb isotopic dating of titanite microstructures: potential
830 implications for the chronology and identification of large impact structures.
831 *Contributions to Mineralogy and Petrology* 173(10) doi:10.1007/s00410-018-1511-0
832 Prior DJ, Boyle AP, Brenker F, Cheadle MC, Day A, Lopez G, Peruzzo L, Potts GJ,
833 Reddy S, Spiess R, Timms NE, Trimby P, Wheeler J, Zetterström L (1999) The
834 application of electron backscatter diffraction and orientation contrast imaging in the
835 SEM to textural problems in rocks. *American Mineralogist* 84:1741-1759
836 Rae ASP, Morgan JVC, G. S. Grieve, R. A. F. Osinski, G. R. Salge, T., Hall B,
837 Ferrière L, Poelchau M, Gulick SPS, Scientists E (2017) Deformation, Shock
838 Barometry, and Porosity Within Shocked Target Rocks of the Chicxulub Peak Ring:
839 Results from IODP-ICDP Expedition 364. In: 48th Lunar and Planetary Science
840 Conference, vol., The Woodlands, Texas, p 1934
841 Rae ASP (2018) *The Kinematics and Dynamics of Complex Crater Collapse*. Imperial
842 College London

1
2
3
4
5
6
7
8
9
10
11
12
13
14
15
16
17
18
19
20
21
22
23
24
25
26
27
28
29
30
31
32
33
34
35
36
37
38
39
40
41
42
43
44
45
46
47
48
49
50
51
52
53
54
55
56
57
58
59
60
61
62
63
64
65

843 Reddy SM, Timms NE, Pantleon W, Trimby P (2007) Quantitative characterization of
844 plastic deformation of zircon and geological implications. Contributions to
845 Mineralogy and Petrology 153(6):625-645 doi:10.1007/s00410-006-0174-4
846 Reddy SM, Johnson TE, Fischer S, Rickard WDA, Taylor RJM (2015) Precambrian
847 reidite discovered in shocked zircon from the Stac Fada impactite, Scotland. Geology
848 43(10):899-902 doi:10.1130/g37066.1
849 Renne PR, Deino ALH, F.J., Kuiper KF, Mark DF, Mitchell WS, Morgan LE, Mundil
850 R, Smit J (2013) Time scales of critical events around the Cretaceous-Paleogene
851 boundary. Science 339(6120):684-687
852 Riller U, Poelchau MH, Rae ASP, Schulte FM, Collins GS, Melosh HJ, Grieve RAF,
853 Morgan JV, Gulick SPS, Lofi J, Diaw A, McCall N, Kring DA, Party I-IES (2018)
854 Rock fluidization during peak-ring formation of large impact structures. Nature
855 562(7728):511-518 doi:10.1038/s41586-018-0607-z
856 Salje E, Schmidt C, Bismayer U (1993) Structural phase transition in titanite,
857 CaTiSiO₅: A Ramanspectroscopic study. Physics and Chemistry of Minerals
858 19(7):502-506
859 Schmieder M, Kring DA, Lapen TJ, Gulick SPS, Stockli DF, Rasmussen C, Rae ASP,
860 Ferrière L, Poelchau M, Xiao L, Wittmann A (2017) Sphene and TiO₂ assemblages in
861 the Chicxulub peak ring: U-Pb systematics and implications for shock pressures,
862 temperatures, and crater cooling. Meteoritics & Planetary Science 52:A308-A308
863 Schulte P, Alegret L, Arenillas I, Arz JA, Barton PJ, Bown PR, Bralower TJ,
864 Christeson GL, Claeys P, Cockell CS, Collins GS (2010) The Chicxulub asteroid
865 impact and mass extinction at the Cretaceous-Paleogene boundary. Science
866 327(5970):1214-1218

1
2
3
4
5
6
7
8
9
10
11
12
13
14
15
16
17
18
19
20
21
22
23
24
25
26
27
28
29
30
31
32
33
34
35
36
37
38
39
40
41
42
43
44
45
46
47
48
49
50
51
52
53
54
55
56
57
58
59
60
61
62
63
64
65

867 Speer JA, Gibbs GV (1976) The crystal structure of synthetic titanite, CaTiOSiO₄,
868 and the domain textures of natural titanites. *American Mineralogist* 61(3-4):238-247
869 Taylor M, Brown GE (1976) High-temperature structural study of the P2₁/a \leftrightarrow A2/a
870 phase transition in synthetic titanite, CaTiSiO₅. *American Mineralogist* 61(5-6):435-
871 447
872 Thomson OA, Cavosie AJ, Moser DE, Barker I, Radovan HA, French BM (2014)
873 Preservation of detrital shocked minerals derived from the 1.85 Ga Sudbury impact
874 structure in modern alluvium and Holocene glacial deposits. *Geological Society of*
875 *America Bulletin* 126(5-6):720-737 doi:10.1130/b30958.1
876 Timms NE, Reddy SM, Healy D, Nemchin AA, Grange ML, Pidgeon RT, Hart R
877 (2012) Resolution of impact-related microstructures in lunar zircon: A shock-
878 deformation mechanism map. *Meteoritics & Planetary Science* 47(1):120-141
879 doi:10.1111/j.1945-5100.2011.01316.x
880 Timms NE, Erickson TM, Zanetti M, Pearce MA, Cayron C, Cavosie AJ, Reddy SM,
881 Wittmann A, Carpenter PK (2017a) Cubic zirconia in >2370 °C impact melt records
882 Earth's hottest crust. *Earth and Planetary Science Letters* 477(1):52-58
883 doi:<https://doi.org/10.1016/j.epsl.2017.08.012>
884 Timms NE, Erickson TM, Pearce MA, Cavosie AJ, Schmieder M, Tohver E, Reddy
885 SM, Zanetti M, Nemchin AA, Wittmann A (2017b) A pressure-temperature phase
886 diagram for zircon at extreme conditions. *Earth Science Reviews* 165:185-202
887 doi:10.1016/j.earscirev.2016.12.008
888 Timms NE, Healy D, Erickson TM, Nemchin AA, Pearce MA, Cavosie AJ (2018)
889 Role of elastic anisotropy in the development of deformation microstructures in
890 zircon. In: Moser D, Corfu F, Reddy S, Darling J, Tait K (eds) *Microstructural*

1
2
3
4
5
6
7
8
9
10
11
12
13
14
15
16
17
18
19
20
21
22
23
24
25
26
27
28
29
30
31
32
33
34
35
36
37
38
39
40
41
42
43
44
45
46
47
48
49
50
51
52
53
54
55
56
57
58
59
60
61
62
63
64
65

891 Geochronology: Planetary Records Down to Atom Scale, Geophysical Monograph
892 232, vol. AGU-Wiley, pp 183-202

893 Wheeler J, Prior D, Jiang Z, Spiess R, Trimby P (2001) The petrological significance
894 of misorientations between grains. Contributions to Mineralogy and Petrology
895 141(1):109-124 doi:10.1007/s004100000225

896 Wheeler J, Mariani E, Piazzolo S, Prior DJ, Trimby P, Drury MR (2009) The weighted
897 Burgers vector: a new quantity for constraining dislocation densities and types using
898 electron backscatter diffraction on 2D sections through crystalline materials. Journal
899 of Microscopy 233(3):482-494

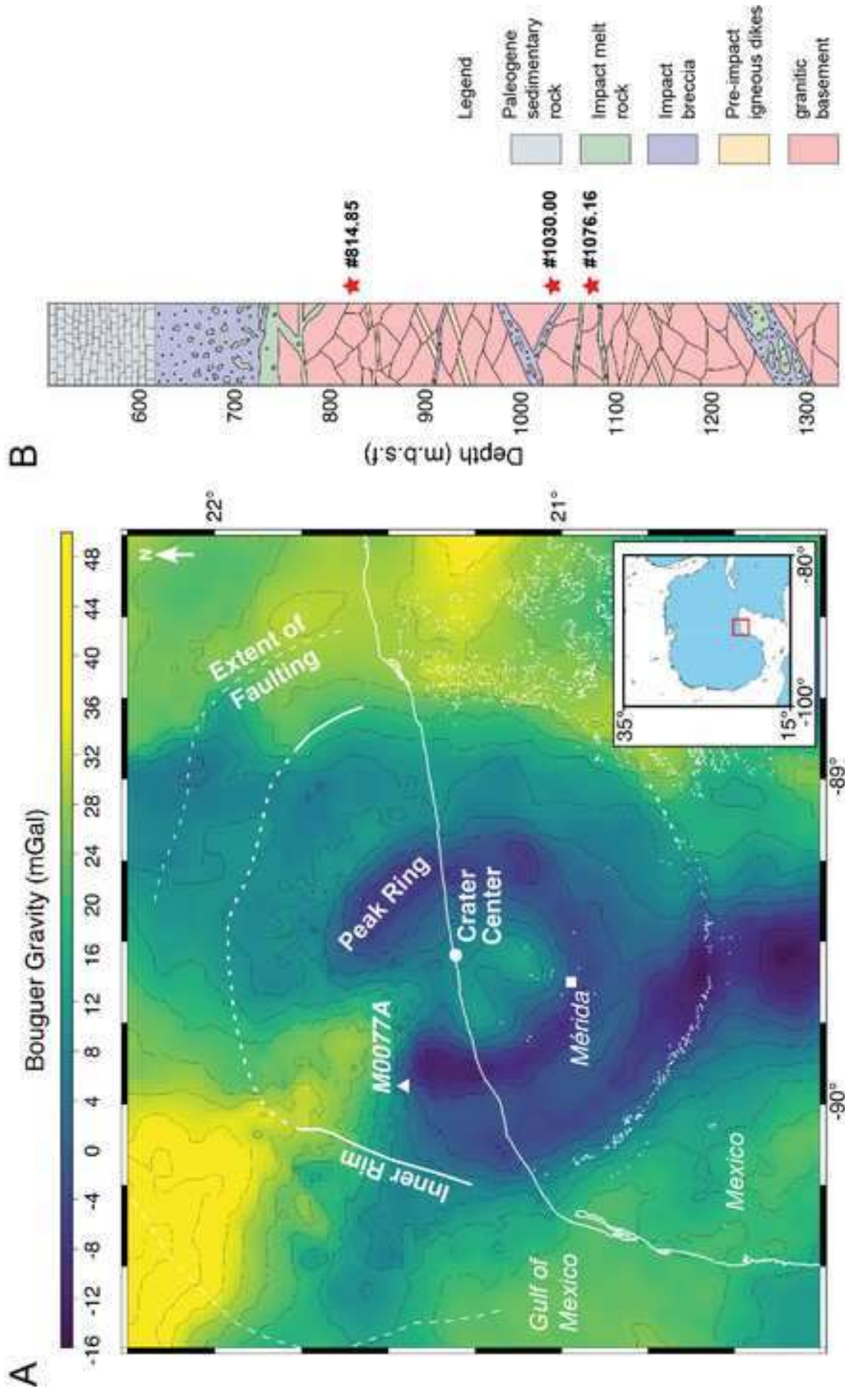
900 White LF, Darling JR, Moser DE, Cayron C, Barker I, Dunlop J, Tait KT (2018)
901 Baddeleyite as a widespread and sensitive indicator of meteorite bombardment in
902 planetary crusts. Geology 46(8):719-722 doi:10.1130/g45008.1

903 Whitney DL, Evans BW (2009) Abbreviations for names of rock-forming minerals.
904 American Mineralogist 95(1):185-187 doi:10.2138/am.2010.3371

905 Wittmann A, Kenkmann T, Schmitt RT, Stöffler D (2006) Shock-metamorphosed
906 zircon in terrestrial impact craters. Meteoritics & Planetary Science 41(3):433-454

907 Zhao JW, Xiao L, Liu HS, Xiao ZY, Morgan J, Gulick S, Kring D, Claeys P, Riller U,
908 Wittmann A, Ferriere L (2017) Shock Metamorphic Effects of the Peak Ring Granites
909 within the Chicxulub Crater. Lunar and Planetary Science Conference Proceedings
910 48:1421

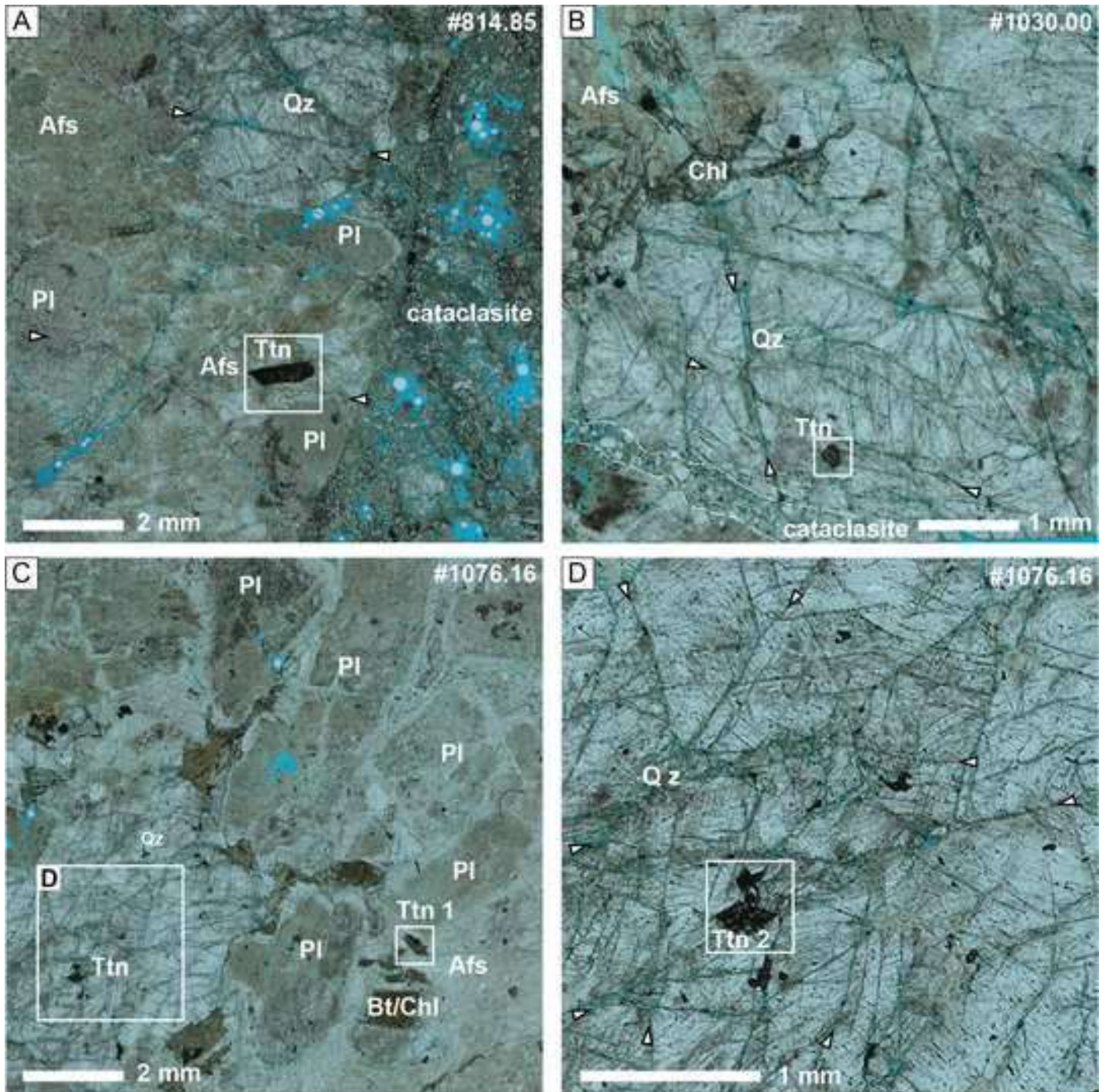
911



Timms Figure 1

Figure 2

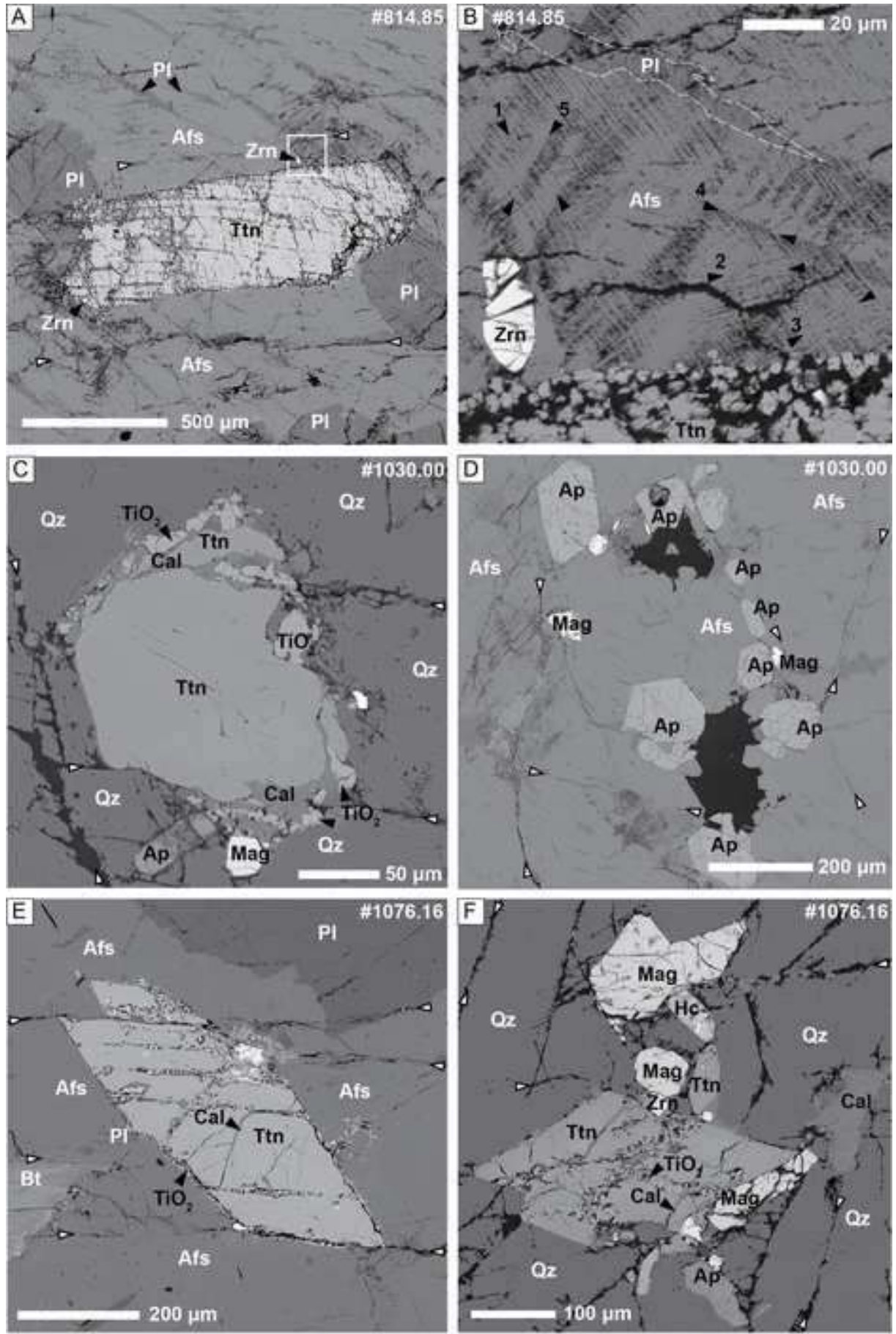
[Click here to access/download;Figure;Timms_ChicxTitaniteMS_Fig02_Optical](#)



Timms Figure 2

Figure 3

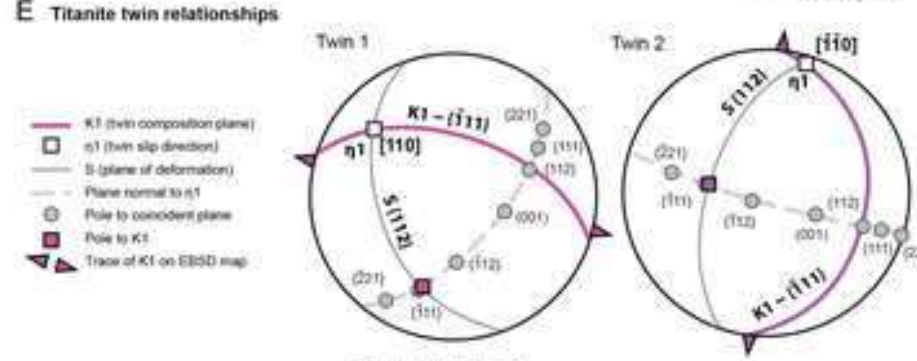
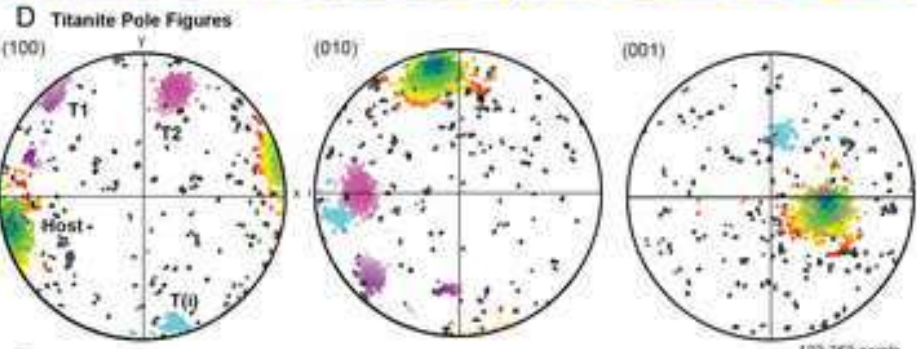
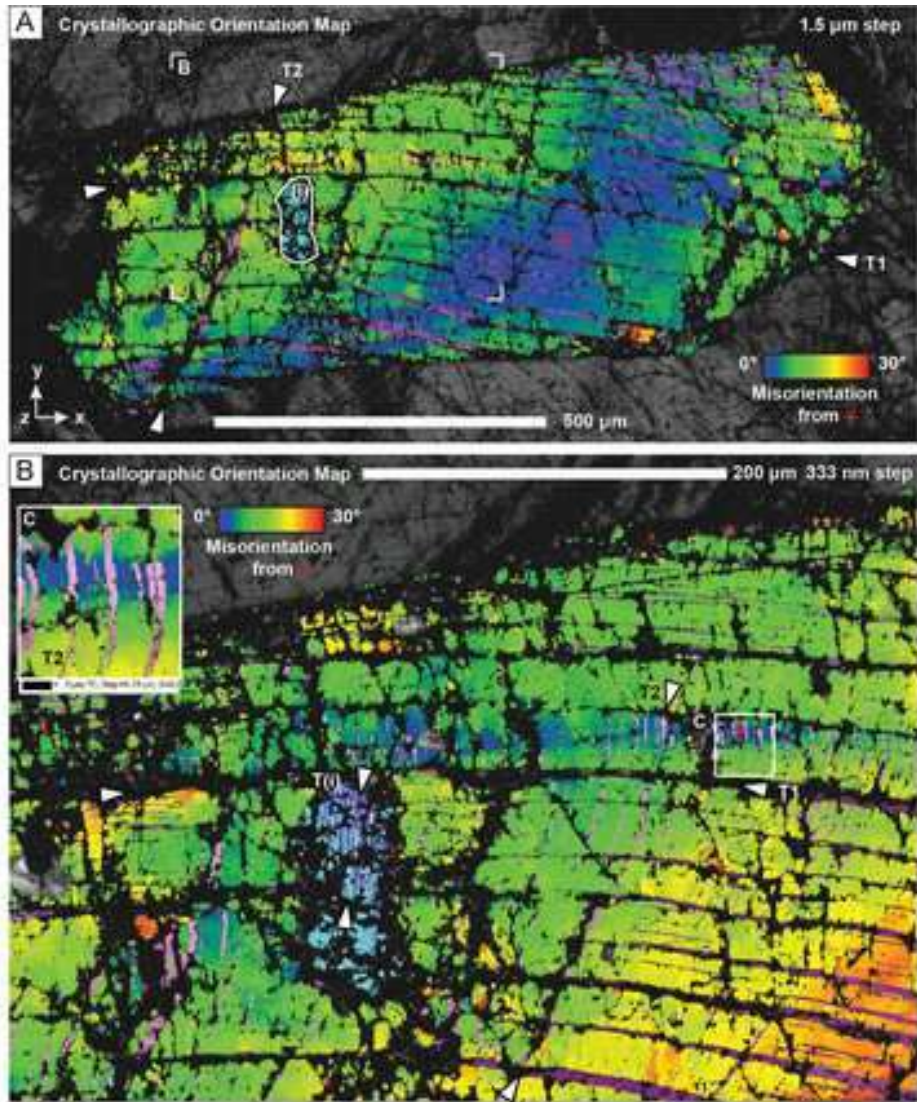
[Click here to access/download;Figure;Timms_ChicxTitaniteMS_Fig03_BSE](#)



Timms Figure 3

Figure 4

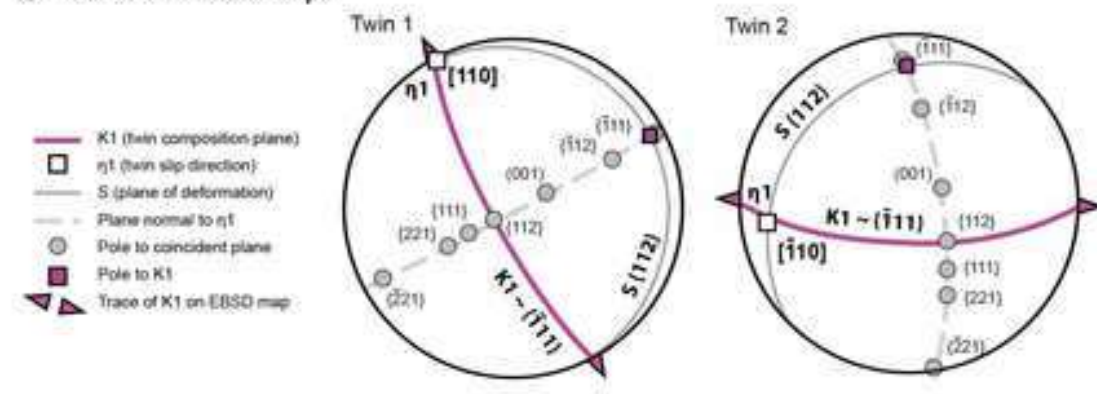
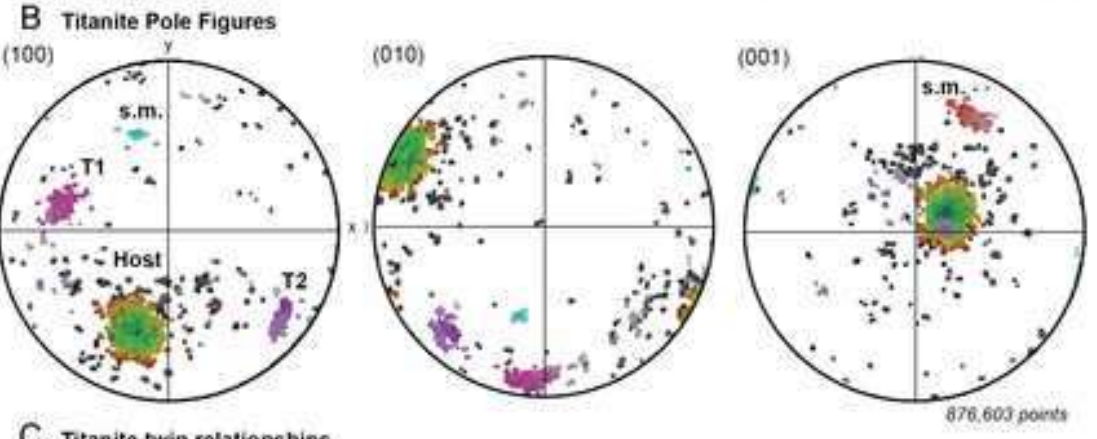
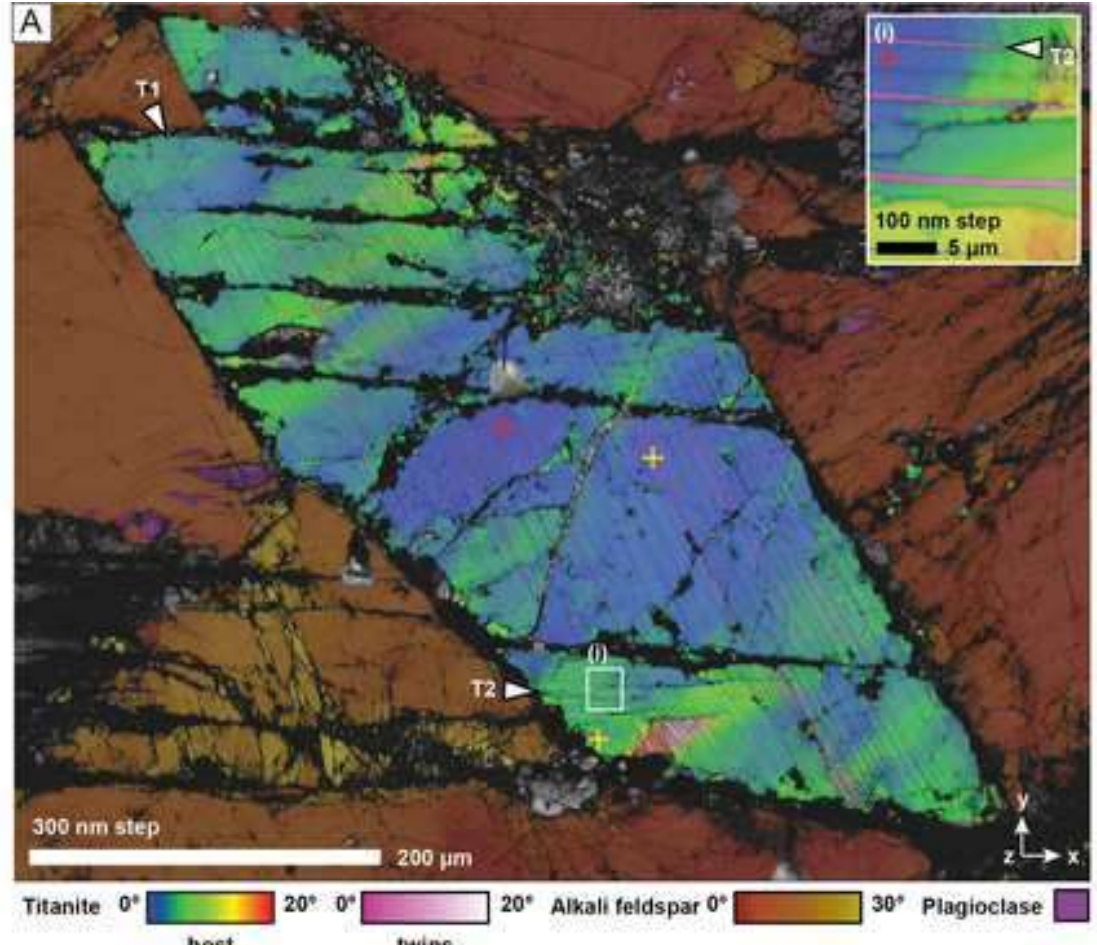
[Click here to access/download;Figure;Timms_ChicxTitaniteMS_Fig04_121_E](#)



Timms Figure 4

Figure 5

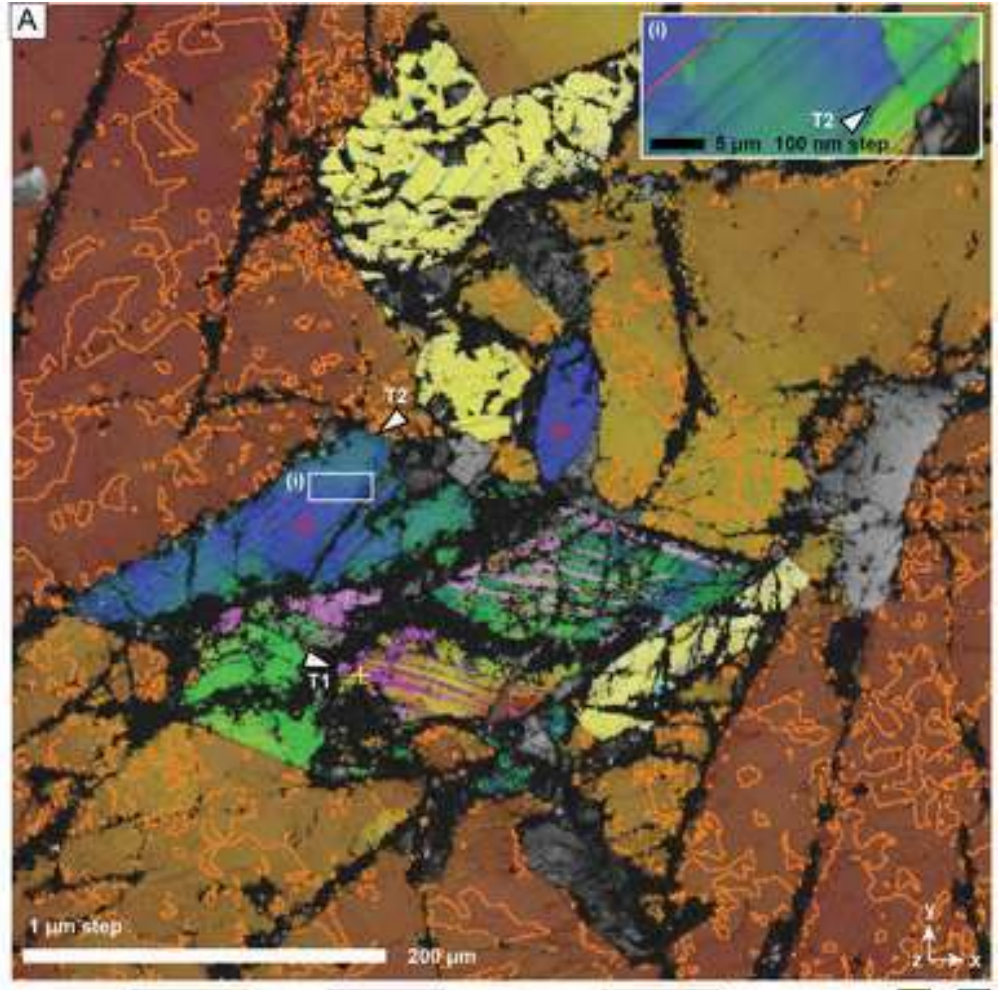
[Click here to access/download;Figure;Timms_ChicxTitaniteMS_Fig05_219_1_](#)



Timms Figure 5

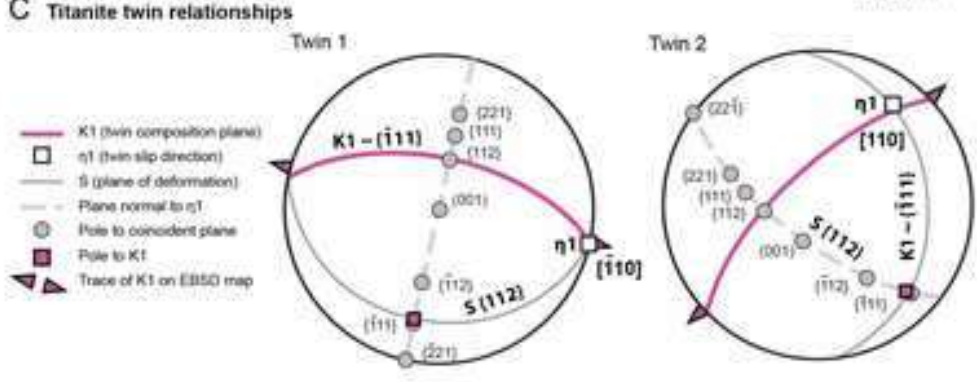
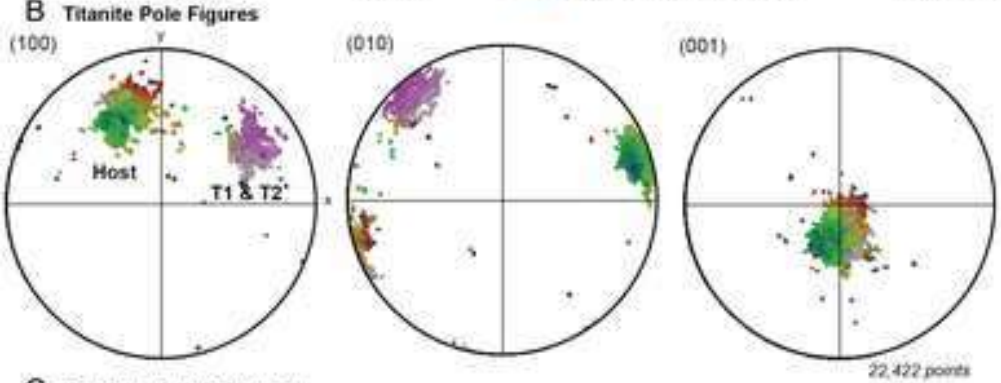
Figure 6

[Click here to access/download;Figure;Timms_ChicxTitaniteMS_Fig06_219_2_](#)



Titanite 0° 30° 0° 30° Quartz 0° 30° Magnetite host twins host twins

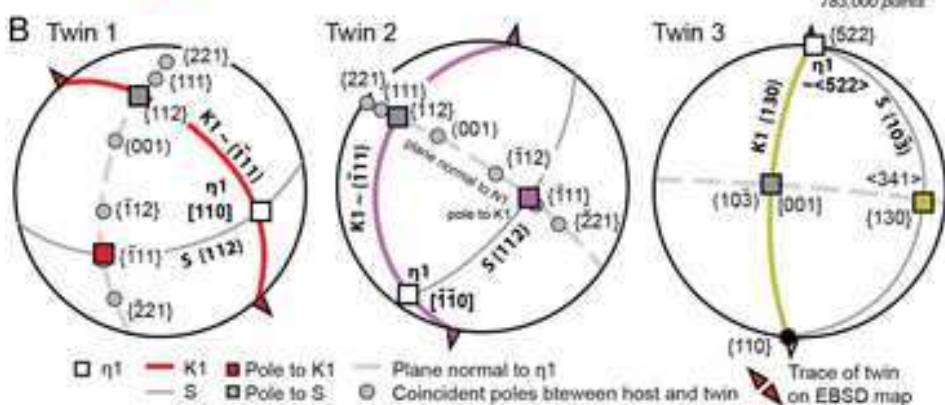
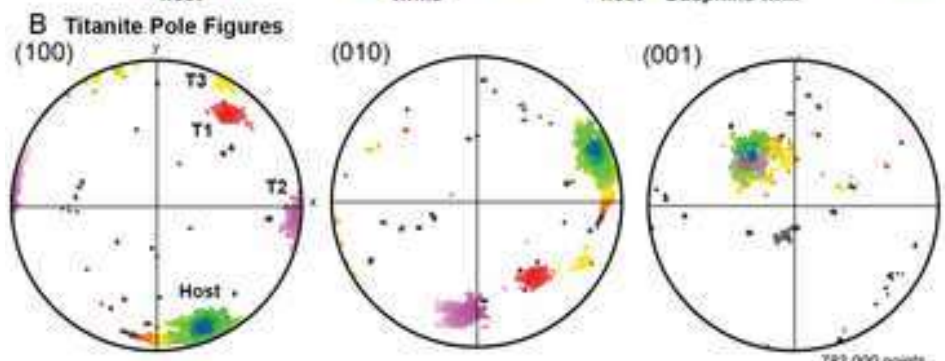
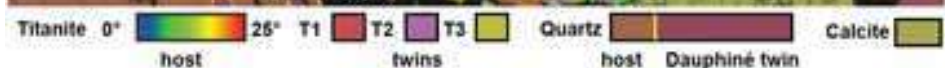
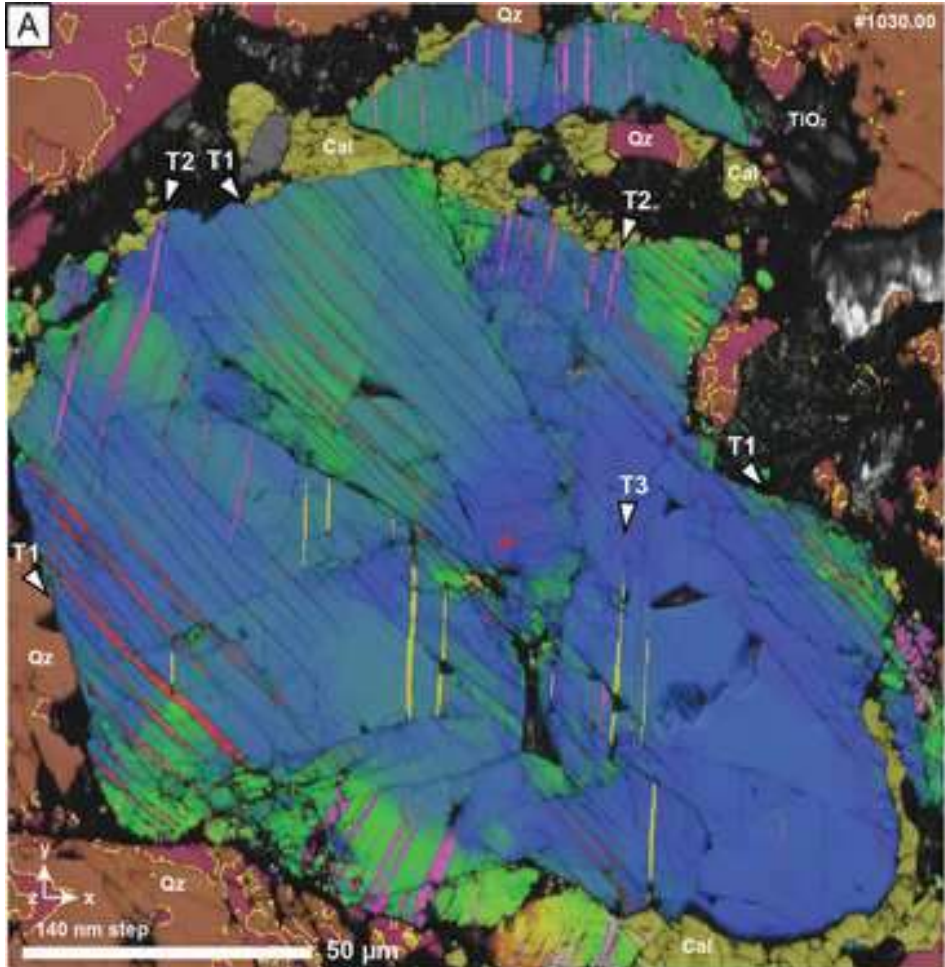
— Dauphiné twin boundary



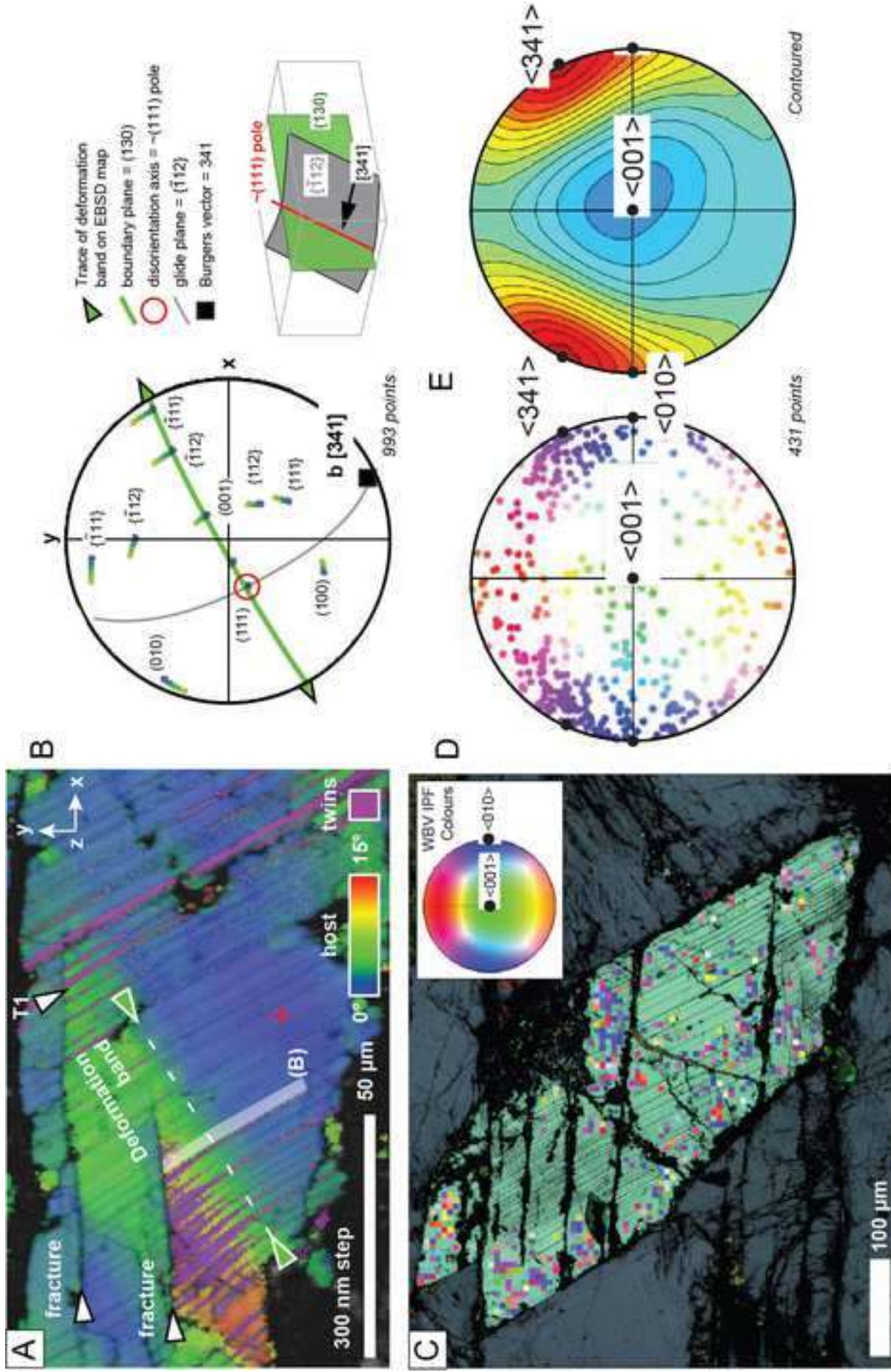
Timms Figure 6

Figure 7

[Click here to access/download;Figure;Timms_ChicxTitaniteMS_Fig07_EBSD](#)



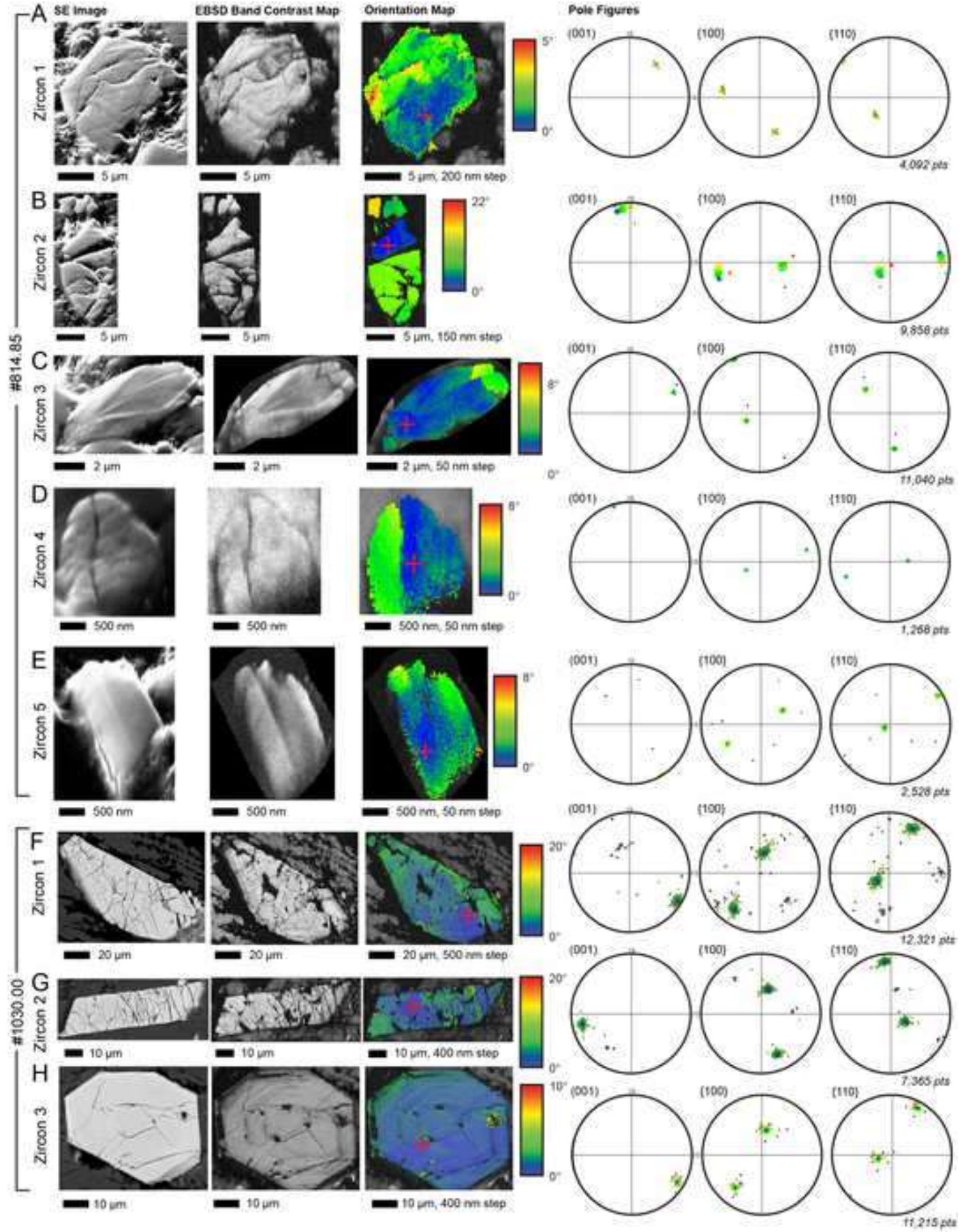
Timms Figure 7



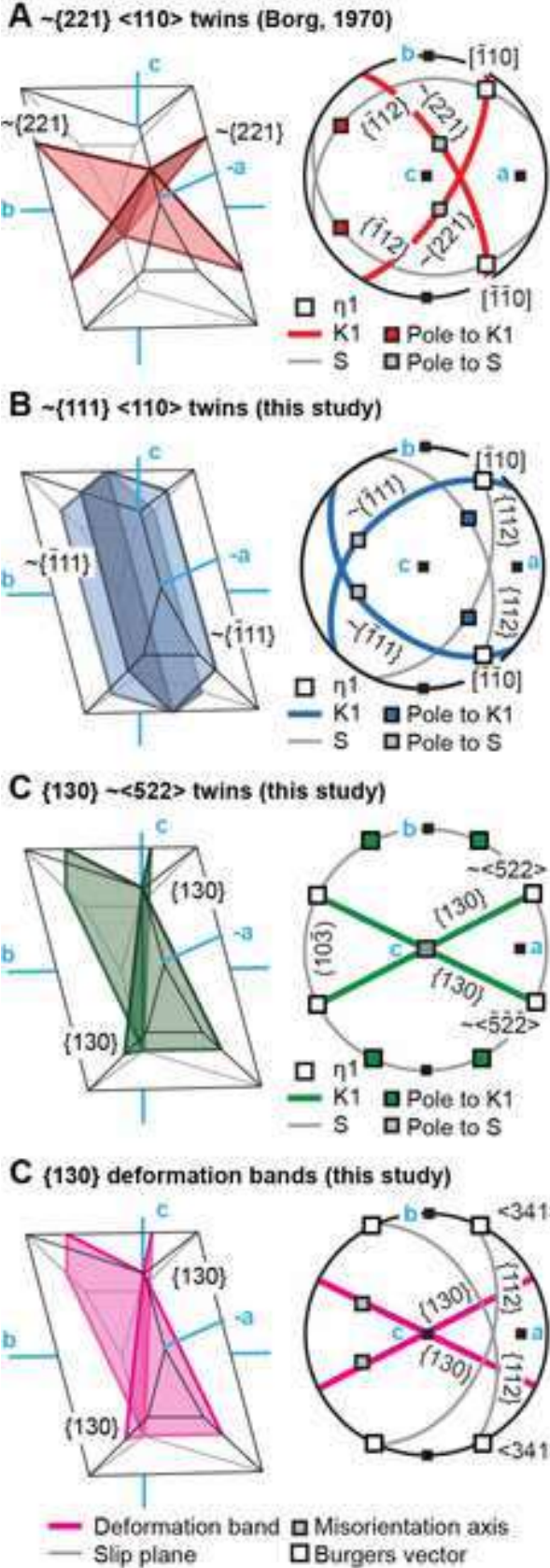
Timms Figure 8

Figure 9

[Click here to access/download;Figure;Timms_ChicxTitaniteMS_Fig09_Zircon](#)



Timms Figure 9



Timms Figure 10

Figure 11

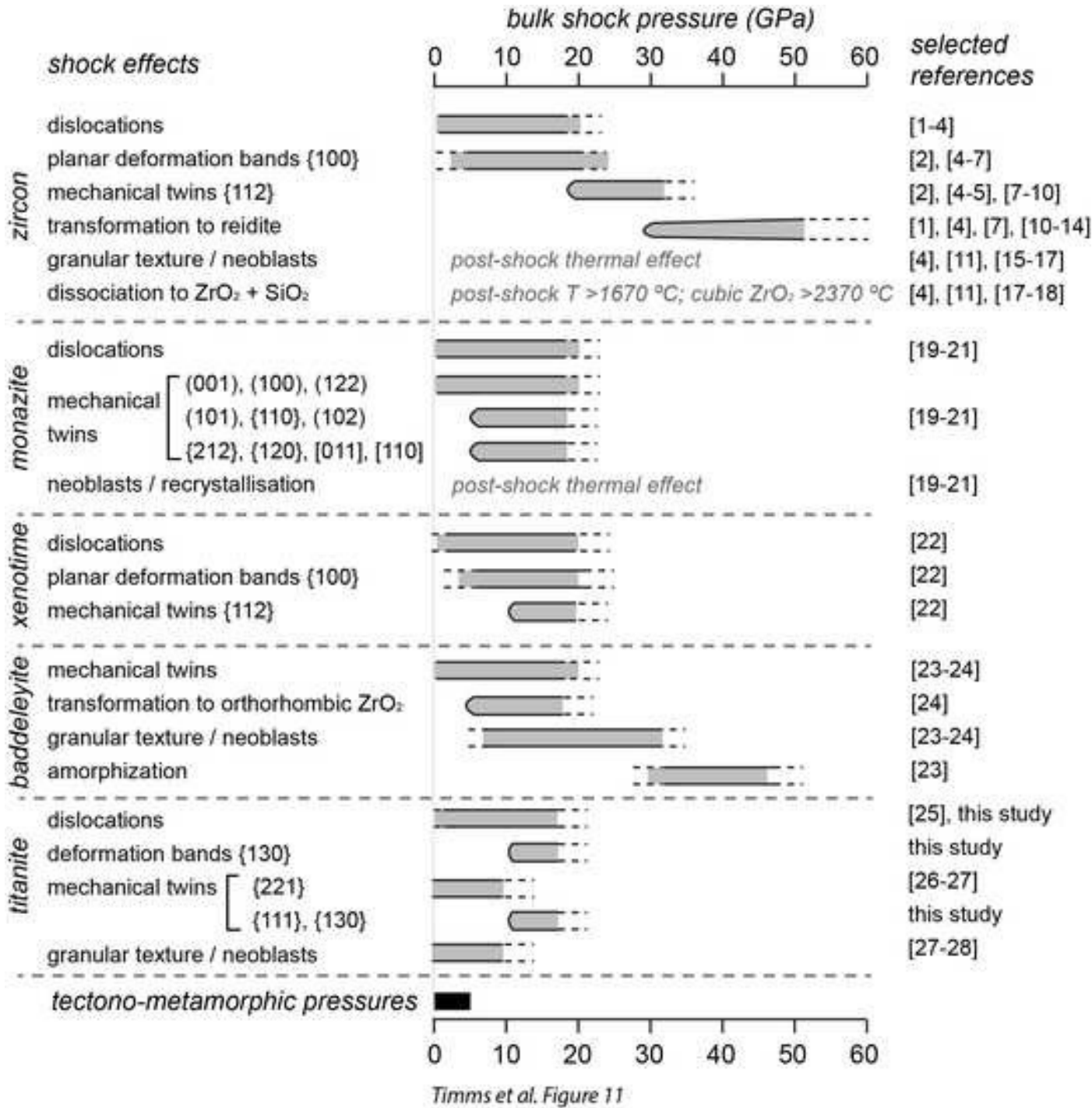


Table 1. Details of samples used in this study. Sample IDs comprise information relating to the IODP catalogue system, and have the following naming convention: Expedition-Site-Hole-Core-Section-TopDepth-BottomDepth. Depths are driller depths given as metres below sea floor (m.b.s.f.).

IODP Sample ID	Depth (m.b.s.f.)	Brief thin section description
364-77-A-121-R-1-75-77	814.85	Shocked granitoid with thick cataclasite bands. Intact domains are dominated by plagioclase and alkali feldspar with perthite lamellae and local PDFs. Subordinate patches of quartz have abundant PFs and PDFs. Minor chlorite after biotite, and euhedral titanite. Accessory apatite, zircon and magnetite. Cataclasite contains patchy calcite cement.
364-77-A-204-R-1-7-9 (duplicate)	1030.00	Shocked granitoid dominated by large plagioclase laths and alkali feldspar with perthite lamellae, subordinate quartz patches with abundant PFs and PDFs. Minor biotite (partially altered to chlorite) and euhedral titanite. Accessory apatite, magnetite, and zircon. Conspicuous set of transgranular planar fractures are lined with calcite.
364-77-A-219-R-1-22-24	1076.16	Shocked granitoid with roughly equal proportions of plagioclase, alkali feldspar and quartz. Quartz contains abundant PFs and PDFs. Minor biotite (heterogeneously altered to chlorite), euhedral titanite and apatite. Accessory magnetite, zircon, and hercynite. Alkali feldspar contains perthite lamellae. Patchy calcite lines fractures.

Table 2. Scanning electron microscopy settings and electron backscatter diffraction analysis acquisition and processing parameters.

SEM			
Make/model		Tescan Mira3 FEG-SEM	
EBSD acquisition system		Oxford Instruments AZtec / Nordlys EBSD Detector	
EDX acquisition system		Oxford Instruments AZtec / XMax 20 mm SDD	
EBSD Processing software		Oxford Instruments Channel 5.10	
Acceleration Voltage (kV)		20	
Working Distance (mm)		18.5	
Tilt		70°	
EBSD match units			
<i>Phase</i>	<i>Space Group</i>	β (°)	
Titanite	15	113.93	American Mineralogist phase database (database family 725, best in family)
Quartz	152	n/a	'Quartznew', HKL database (Sands, 1969)
Orthoclase	12	116.07	American Mineralogist phase database (Prince et al., 1973)
Bytownite	2	115.87	ICSD phase database (Facchinelli et al., 1979)
Magnetite	227	n/a	HKL phase database (Wechsler et al., 1984)
Calcite	0	n/a	HKL phase database (calcite.cry)
Zircon	141	n/a	Zircon5260, 1 atm (Hazen and Finger, 1979)
Reidite	88	n/a	Reidite6032 0.69 GPa (Farnan et al., 2003)
Apatite	176	n/a	ICSD phase database (Gankev, 1996)
EBSP Acquisition, Indexing and Processing			
EBSP Acquisition Speed (Hz)	40	Band detection (min / max)	6 / 8
EBSP Background (frames)	64	Mean mean angular deviation (all phases)	<1°
EBSP Binning	4 x 4	Wildspike correction	Yes
EBSP Gain	High	Nearest neighbor zero solution extrapolation	8
Hough resolution	60		

Table 3. Unit cell parameters for titanite

A (Å)	6.554
B (Å)	8.708
C (Å)	7.069
α (°)	90
β (°)	113.93
γ (°)	90

Table 4. Host-twin disorientation and misorientation calculations for titanite

Grain and twin ID	Disorientation		180° Misorientation				
			Angle	Best fit plane normal		Best-fit direction	
	Angle (°)	Axis <hkl>	(°)	Plane {hkl}	Deviation (°)	Axis {hkl}	Deviation (°)
121 T1	75.23	102	179.92	$\bar{1}\bar{1}0$	0.66	$2\bar{4}\bar{1}$	4.53
121 T2	72.27	$\bar{1}0\bar{2}$	179.33	$\bar{1}\bar{1}0$	1.59	$2\bar{4}\bar{1}$	2.60
121 T(i)	73.32	102	179.34	$\bar{1}\bar{1}0$	0.67	$2\bar{4}\bar{1}$	4.01
204 T1	74.16	102	179.98	110	0.23	$2\bar{4}\bar{1}$	4.12
204 T2	74.02	102	179.65	$\bar{1}\bar{1}0$	0.22	$2\bar{4}\bar{1}$	4.07
204 T3	51.30	001	179.97	$\bar{3}\bar{4}\bar{1}$	2.11	$\bar{1}\bar{3}0$	0.20
219_1 T1	73.93	$\bar{1}0\bar{2}$	179.93	$\bar{1}\bar{1}0$	0.08	$2\bar{4}\bar{1}$	3.88
219_1 T2	74.17	$\bar{1}0\bar{2}$	176.85	$\bar{1}\bar{1}0$	0.73	$2\bar{4}\bar{1}$	4.37
219_2 T1	72.12	102	178.20	110	1.06	$2\bar{4}\bar{1}$	3.53
219_2 T2	72.58	102	179.98	$\bar{1}\bar{1}0$	0.75	$2\bar{4}\bar{1}$	3.18
Borg 1970	~73	102	180	110	n/a	221	n/a

Table 5. Twinning in titanite. Disorientation = angle/axis that describes the minimum misorientation between the twin and the host. 'Coincidence' is defined as $<0.7^\circ$ angular deviation.

Source Reference	Borg (1970)	Borg (1970)	This study	This study
Examples			#814.85 (T1, T2), #1030.00 (T1, T2), #1076.16_1 (T1, T2), #1076.16_2 (T1, T2)	#1030.00 (T3)
Twin Mode				
K ₁ (slip plane, plane of no distortion, composition plane)	Irrational ~{221}	{ $\bar{1}31$ }	Irrational ~{ $\bar{1}11$ }	{130}
η_1 (Slip direction)	$\langle 110 \rangle$	Irrational	$\langle 110 \rangle$	Irrational ~ $\langle 522 \rangle$
K ₂ (Conjugate plane of no distortion)	{ $\bar{1}31$ }	Irrational ~{221}	Rational ???	???
η_2 (axis of principal zone)	Irrational	$\langle 110 \rangle$???	???
S (plane of deformation)	Irrational ~{ $\bar{1}12$ }		{112}	($\bar{1}03$)
Twin type	2	1	2	1
Disorientation				
Angle	~74°	~74°	~74°	~53°
Axis	$\langle 102 \rangle$	$\langle 102 \rangle$	$\langle 102 \rangle$	[003]
Coincident Planes				
(001)			Yes	No
{111}			Yes	No
{ $\bar{1}11$ }			Yes	No
{112}			Yes	No
{ $\bar{1}12$ }			Yes	No
{221}			Yes	No
{22 $\bar{1}$ }			Yes	No
{24 $\bar{1}$ }			(Yes?)	No
{130}			No	Yes
($\bar{1}03$)			No	Yes
Coincident directions				
[001]			No	Yes
$\langle 110 \rangle$			Yes	No
$\langle \bar{1}10 \rangle$			Yes	No
$\langle 34\bar{1} \rangle$			No	No